Annu. Rev. Phys. Chem. 2018. 69:327–352 https://doi.org/10.1146/annurev-physchem-052516-050602 Copyright © 2018 by Annual Reviews. All rights reserved *Jonas* 

www.annualreviews.org • Vibronic Coherence in 2D Spectroscopy

# Vibrational and Nonadiabatic Coherence in 2D Electronic Spectroscopy, the Jahn–Teller Effect, and Energy Transfer

David M. Jonas

Department of Chemistry and Biochemistry, University of Colorado, Boulder, Colorado 80309-0215, USA; email: david.jonas@colorado.edu

## **Abstract**

Femtosecond two-dimensional (2D) Fourier transform spectroscopy generates and probes several types of coherence that characterize the couplings between vibrational and electronic motions. These couplings have been studied in molecules with Jahn–Teller conical intersections, pseudo-Jahn–Teller funnels, dimers, molecular aggregates, photosynthetic light harvesting complexes, and photosynthetic reaction centers. All have closely related Hamiltonians and at least two types of vibrations, including one that is decoupled from the electronic dynamics and one that is nonadiabatically coupled. Polarized pulse sequences can often be used to distinguish these types of vibrations. Electronic coherences are rapidly obscured by inhomogeneous dephasing. The longest-lived coherences in these systems arise from delocalized vibrations on the ground electronic state that are enhanced by a nonadiabatic Raman excitation process. These characterize the initial excited-state dynamics. 2D oscillation maps are beginning to isolate the medium lifetime vibronic coherences that report on subsequent stages of the excited-state dynamics.

1

## INTRODUCTION

Very soon after the the first two-dimensional Fourier transform (2DFT) electronic spectra(1) and theory(1a) were reported, it was recognized that electronic coupling to the vibrational and environmental motions (2-4) that lie at the heart of chemistry (5-7) posed challenges for their interpretation. The challenges arise because 2DFT spectroscopy uses femtosecond pulses (8-11), which are faster than the vibrational and environmental motions that broaden electronic transitions. Interpretation (2, 4, 12) required extending the framework of 2DFT NMR spectroscopy (13) in order to incorporate the femtosecond capture of these motions, essential for chemical reactivity, as frozen (14-17). In electronic spectroscopy and dynamics, vibrations can be separated into two types on the basis of whether or not they are involved in coupling different electronic states together. The nonlinear optical response theory developed by Mukamel (18) and coworkers was used to treat the effects of vibrations and environmental motions that do not couple electronic states together in 2D electronic spectroscopy (4, 12, 19, 20). Reviews since that time cover purely electronic theory (21) and experimental approaches (22). This review emphasizes nonadiabatically coupled vibrations that drive changes in electronic state and their manifestations in 2DFT electronic spectra.

A great deal of work in this broad area has been concerned with electronic coupling and electronic energy transfer between light absorbing chromophores, but similar questions arise in charge transfer and internal conversion. Many charge transfer processes depend on absolute electronic energies, so that determination of the fundamental energetics can require electrochemical measurements. Internal conversion processes often involve spectroscopically dark states that are similarly challenging to characterize. The energetics of electronic energy transfer are more readily and precisely accessible because they depend on intramolecular energy gaps of donor and acceptor that can be measured spectroscopically. This allows more stringent tests of theory. It has long been known that Jahn–Teller effects involve related Hamiltonians, for which analysis can be further simplified by symmetry.

The basic framework of energy transfer theory is due to Förster (23), and has well-understood strong coupling and weak coupling limits. However, many very efficient energy transfer processes (including much of photosynthetic energy transfer) operate in a less-understood intermediate coupling regime(23a) between these limits. In all of these processes, there is a complex interplay between electronic energies, electronic couplings, environmental

motions, and intramolecular vibrations. Experimentally, this is further complicated by time averaging over fluctuations or ensemble averaging over disorder (or both). Single-molecule spectroscopy removes the ensemble average but always averages over slow fluctuations during repeated measurements (24–26). Ensemble-averaged 2DFT spectroscopy correlates frequencies within each molecule at a precisely defined time delay (2) and is uniquely sensitive to coherent dynamics.

Beneath this averaging, the role of the environment in the dynamics is intrinsically complicated because each system interacts with its environment before stabilizing products and reaching thermal equilibrium. For measurements that probe only part of a system directly, a reduced description can be useful. Because part of an interacting system does not even have a wavefunction (27), such a description starts from the density matrix  $\hat{\rho} = |\psi\rangle\langle\psi|$  and eliminates the bath degrees of freedom by taking a partial trace over them (27, 28). This reduced density matrix can be used to calculate any measurement that depends only on the system degrees of freedom. However, through system—bath interactions, the evolution of the reduced density matrix makes a transition from coherent quantum dynamics to dissipative level kinetics in some preferred basis [the pointer basis (29) preferred by the interacting system, bath, and measurement]. Coherence decay or decoherence (30–32) quantifies this transition in the evolution of the system we can measure (see the sidebar titled decoherence).

The decoherence timescale  $\tau_{\rm dec}$  matters for chemical reaction rates because it breaks up the coherent quantum evolution into chunks of length  $\tau_{\rm dec}$ . For a two-level system, coherent quantum dynamics is characterized by cosinusoidal Rabi flopping back and forth between basis states under the influence of a coupling (33). Through constructive interference, the small quantum population transfer is proportional to  $t^2$ , so each coherent chunk of time has a quantum population transfer proportional to  $t^2$ , with the consequence that the rate constant is proportional to  $t^2$  as long as  $t^2$  is much less than the coherent Rabi flopping frequency (23). For longer  $t^2$ , the rate constant has a Rabi maximum (34) when the product energy relaxation rate is matched to the Rabi flopping frequency (35). Much richer dynamics are possible (36, 37).

Theoretical studies often use a definition of electronic coherence that traces over all vibrational degrees of freedom (32, 38, 39). Experimentally, this definition corresponds to the nonselective polarization dephasing measured by detection of the two-pulse photon echo energy

using transform-limited excitation pulses with spectra that span the absorption transition (40). For room-temperature molecular electronic transitions in condensed phases, this timescale is typically dominated by vibrational broadening of the electronic band and can be on the order of 10 fs or less. This fast decay arises from destructive interference among a sum of oscillations with a broad span of frequencies. The decay of interference between the electronic ground and excited state measured by 2DFT spectroscopy is slower because one frequency is selected within the electronic band, but interference still typically survives for only about 100 fs (3). This is the electronic decoherence timescale most often reported from 2DFT experiments. This optical decoherence timescale is not necessarily the same as the corresponding timescale for decoherence between two excited electronic states (1a, 21). Vibronic decoherence will be slower because it involves a more complete specification of the system states (41). Finally, molecular vibrational coherence on a single electronic state typically survives for over 1 ps (15).

The questions that have arisen in the studies reviewed here concern the dynamics of spontaneous transitions between electronically excited states, with emphasis on the role of vibrations and the environment. The most important questions concern the mechanism for spontaneous electronic transitions in Jahn–Teller dynamics, internal conversion, energy transfer, and charge transfer. Resolving these requires an understanding of how electronic, vibrational, and environmental motions are reflected in 2DFT spectra and obscured by disorder. Nonadiabatic coupling between vibrational and electronic motions can lead to deceptively similar vibrational 2DFT signatures that were initially misinterpreted as long-lived (picosecond) electronic coherence in many coupled electronic systems, especially photosynthetic antenna complexes. The similarities include complete sequences of frequencies and polarizations, as well as parts of the patterns for which 2D peaks have quantum beats. However, electronic coherence and nonadiabatically excited vibrations require different regimes for molecular parameters that can be independently measured and also produce differences in the overall 2D quantum beat patterns. Evidence has been rapidly accumulating that nonadiabatic couplings enhance particular vibrations in 2DFT spectra, which readily explains the picosecond decoherence. This raises new questions about nonadiabatic energy transfer mechanisms.

## 2D FOURIER TRANSFORM ELECTRONIC SPECTRA

2DFT spectra are recorded by exciting the sample with systematically varied sequences of short

pulses of light (3,4,22). For each pulse sequence, the measured signal must arise from a nonlinear response to all of the pulses in that pulse sequence. The nonlinear response is understood by considering how the electric fields of all the light pulses interact with a molecule's wavefunction. **Figure 1** shows one sequence of three pulses and a radiated signal field. Since fields are amplitudes for photon number states, incoherent processes involving four fields can be considered as two-photon processes (for example, absorption of one photon to populate one excited state followed by incoherent relaxation to populate a lower state before subsequent radiation of another photon). Unless the relaxation time *T* greatly exceeds the longest decoherence time, a coherent wave picture is needed for both molecule and fields. The easiest way to make sure the signal depends on all three pulses is to focus parallel beams on three corners of a square into the sample and then detect the signal field that emerges on the fourth corner (1). This widely used method(22) requires a fourth pulse for interference detection of the signal field, but uniquely defines the relative signs of the frequencies through phase matching, detects changes in both absorption and refraction, and allows independent control of the polarization for each pulse.

In isotropic media, there are three independent elements of the nonlinear response tensor (42) and three polarization sequences (43) that measure population (the isotropic signal measured at the magic angle), orientation (the difference between up and down), and alignment (the difference between up/down and right/left measured by the polarization anisotropy) (44–47). The all-parallel and the  $(-\pi/4, \pi/4, \pi/2, 0)$  polarization sequence (43) are most often used (48, 49). The orientational average for a given sequence of molecular transition dipoles and pulse polarizations depends on a cyclic set of transition dipoles (50) and can be calculated using equation 10 of Reference 51. Group theory can determine symmetries from the two-photon tensor (52).

Real 2D relaxation spectra establish that excitation at  $\omega_{\tau}$  causes a subsequent increase (positive signal) or decrease (negative signal) in light transmitted through the sample at  $\omega_{t}$ . Because 2D spectra are measured from the signal field and Fourier transforms are linear, the 2D spectrum for an ensemble is obtained by adding the 2D spectra for all molecules in the ensemble (this is not true for absolute value 2D spectra). Inhomogeneous dephasing from this addition can be eliminated by rephasing with opposite frequencies during  $\tau$  and t, but inhomogeneous dephasing is not removed for oscillations during the one relaxation time T (3).

Figure 2 shows part of the 2DFT spectrum for a model dimer (105). The changes in transmission detected in 2D spectra can arise from three effects after the excitation pulse pair excites some fraction of molecules: Stimulated emission from molecules in the excited state effectively increases sample transmission [positive signal from excited-state emission (ESE)]; the corresponding depletion of the ground state decreases sample absorption [positive signal from ground-state bleaching (GSB)]; and molecules in the excited state can absorb light in transitions to higher-lying states [negative signal from excited-state absorption (ESA)]. Figure 2 shows only the real part of the GSB signal for a rephasing pulse sequence, where  $\omega_t$  and  $\omega_\tau$ have opposite signs. However, rephasing scans are incomplete, covering only positive  $\tau$ , so the discontinuity at  $\tau = 0$  generates ringing artifacts visible as negative regions. The key feature in Figure 2 is the set of four resolved positive peaks. Two peaks lie on the diagonal, with  $\omega_t \approx -\omega_\tau \approx 11,480 \text{ cm}^{-1}$  and 11,680 cm<sup>-1</sup>, respectively. These frequencies match the two maxima in the electronic absorption spectrum of the dimer. These diagonal peaks arise because exciting a transition depletes the ground state for that transition. There are also two off-diagonal cross peaks in which the frequency of each transition is cross-matched with the other. These arise because the two transitions in the dimer share a common ground state, so that exciting one depletes the ground state for the other, and vice versa. The complete rephasing 2DFT spectrum would include four more peaks from ESE plus four more peaks from ESA.

All four peaks are elongated parallel to the diagonal, partly because different dimers in the ensemble have different electronic excitation energies (inhomogeneous broadening). The peak cross-widths perpendicular to the diagonal reflect homogeneous broadening intrinsic to a single dimer, but are also distorted by ringing. Absorption-mode 2DFT spectra can be recorded using scans that cover positive and negative  $\tau$  to balance rephasing versus nonrephasing coherence and minimize ringing (1, 2). The cross-width perpendicular to the diagonal in absorption-mode 2DFT spectra measures optical decoherence between the ground and excited electronic states for a selected diagonal frequency (4, 19). This decoherence timescale is typically on the order of ~100 fs for molecules in room-temperature solution (3).

# QUANTUM BEATS AND INHOMOGENEOUS DEPHASING

In 2DFT spectra, molecular coherence manifests as oscillatory changes in peak amplitude, peak

shape, or both as a function of the relaxation time. The oscillatory beats in 2DFT spectroscopy are a type of quantum beat  $(\underline{53}-\underline{58})$ , much as occurs in emission after excitation of a coherent superposition state with a transform-limited pulse. If the pulse coherently excites state 0 to states 1 and 2 and the emission lines are not distinguished at the detector, then interference can be detected. For a single molecule, the time-dependent emission probability back to state 0 has the form  $(\underline{59}$ , equation 13.6 with  $\phi = 0$ ; see also  $\underline{57}$ )

$$I(t;\Delta) = I_{1-0}(t) + I_{2-0}(t) + 2\sqrt{I_{1-0}(t)I_{2-0}(t)}\cos(\Delta t), \tag{1}$$

where  $I_{1-0}(t)$  is the 1–0 emission probability. The last term is quantum beating of the emission at  $\Delta = \omega_{21} = (\omega_{20} - \omega_{10})$ , the difference between excitation frequencies. If the inhomogeneous broadening of  $\omega_{20}$  and  $\omega_{10}$  is fully correlated so that the splitting  $\omega_{21}$  is constant, the quantum beats are unaffected by ensemble averaging. This often occurs in solution, where vibrational frequencies are almost unaffected by electronic inhomogeneities that obscure the vibrational progression (11, 60). Transient absorption quantum beats decay by dephasing between the excited states (60).

If the splitting  $\omega_{21}$  varies across the ensemble, then the addition of cosines with different beat frequencies will cause faster quantum beat decay (dephasing). This total dephasing between two states in an ensemble of systems is necessarily as fast as, or faster than, the decoherence between those two states in the individual systems within the ensemble. Since each system is characterized by an average transition frequency and a splitting, the ensemble has some joint probability distribution  $p(\omega, \Delta)$ . The marginal distribution of average frequencies is

$$p_{\omega}(\omega) = \int p(\omega, \Delta) d\Delta$$
 (2)

and reflects only correlated inhomogeneity, while the marginal distribution of splittings

$$p_{\Delta}(\Delta) = \int p(\omega, \Delta) d\omega$$
 (3)

reflects only anticorrelated inhomogeneity. Averaging the quantum beats in Equation 1 over this distribution gives

$$\begin{split} \left\langle I(t) \right\rangle &= \iint I(t;\Delta) p(\omega,\Delta) \mathrm{d}\omega \mathrm{d}\Delta = \int I(t;\Delta) p_{\Delta}(\Delta) \mathrm{d}\Delta \\ &= I_{1-0}(t) + I_{2-0}(t) + 2 \sqrt{I_{1-0}(t)I_{2-0}(t)} \int p_{\Delta}(\Delta) \cos(\Delta t) \mathrm{d}\Delta. \end{split} \tag{4}$$

The integral in the last term is the Fourier cosine transform of the splitting marginal,  $p_{\Delta}(t) = \int p_{\Delta}(\Delta) \cos(\Delta t) d\Delta \text{ , which hastens ensemble average quantum beat decay through inhomogeneous dephasing of the anticorrelated inhomogeneity. This type of inhomogeneous quantum beat decay was proposed by Savikhin et al. (61) as the explanation for a 140–180 fs decay of excitonic quantum beats in the femtosecond pump–probe polarization anisotropy of the FMO (Fenna–Matthews–Olson) antenna protein at 19K. These anisotropy beats had large amplitudes of 0.1–0.2 in comparison to the subsequent relaxed anisotropies of ~0.3. [For reference, the standard dipolar anisotropy is 0.4 and the maximum possible anisotropy beat amplitude for a dimer with two equal and orthogonal transition dipoles is 0.3 (50, 62, 63).] For a Gaussian decay of the excitonic quantum beats, <math>p_{\Delta}(t) = \exp[-\sigma_{\Delta}^2 t^2/2]\cos(\Delta_0 t)$ , this yields a Gaussian inhomogeneous distribution of excitonic splittings,

$$p_{\Delta}(\Delta) = (2\pi\sigma_{\Delta}^2)^{-1/2} \exp[-(\Delta - \Delta_0)^2 / 2\sigma_{\Delta}^2].$$

Using the formalism of References <u>21</u>, <u>64</u>, <u>65</u>, this can be generalized to dynamic splittings for both dimers and square symmetric molecules with Jahn–Teller distortions (66–68), yielding

$$p_{\lambda}(t) = \cos(\Delta_0 t) \exp[-4g_{\lambda}(t)], \quad (5)$$

where  $g_{\Delta}(t)$  is the anticorrelated lineshape function. In the high-temperature limit,  $g_{\Delta}(t) = \sigma_{\Delta}^2 \int_0^t \mathrm{d}t' \int_0^{t'} \mathrm{d}t'' M_{\Delta}(t'')$  depends on the variance of the anticorrelated splitting  $[\sigma_{\Delta}^2]$  and the double integral of the normalized correlation function for the anticorrelated splitting  $[M_{\Delta}(t)]$ . The low-temperature lineshape function is given in References 69, 70. Since the correlation function is normalized at t=0, a high time resolution measurement of the quantum beat decay can provide separate information about the splitting distribution and its correlation function (81)now(70a). Since  $M_{\Delta}(t)$  decays from  $M_{\Delta}(0) = 1$ , anticorrelated fluctuations actually slow the quantum beat decay compared to a static splitting distribution.

# JAHN-TELLER DYNAMICS

# Symmetric/Asymmetric and Correlated/Anticorrelated Vibrations

Jahn & Teller (71) showed that the electronic potential energy surfaces for orbitally degenerate electronic states lift the degeneracy by adopting a lower-symmetry geometry. In a Jahn–Teller system, vibrational normal modes can be rigorously classified according to their point-group symmetry. Only totally symmetric vibrations are Franck–Condon active in absorption and emission. Totally symmetric vibrations have exactly the same effect on both Jahn–Teller degenerate states and play no role in coupling them or destroying coherence between them. Only certain asymmetric vibrations are involved in Jahn–Teller distortions toward lower-symmetry molecular geometries. The Jahn–Teller active asymmetric vibrations can couple electronic states to transfer population or tune their energies in opposite directions to destroy coherence. A similar interaction, the pseudo-Jahn–Teller effect, occurs for nearly degenerate electronic states (72). The Hamiltonians for energy transfer and pseudo-Jahn–Teller coupling are interconverted by an electronic basis set transformation (73–75).

Viewing donor and acceptor together as one supermolecule, electronic energy transfer is a kind of internal conversion ( $\frac{76}{100}$ ) (105). This analogy suggests that intramolecular vibrations of the supermolecule play a dominant energetic role, just as they do in internal conversion (77). In a degenerate homodimer, symmetry requires that the intramolecular vibrations of the dimer be delocalized linear combinations of the monomer vibrations that are symmetric or antisymmetric under exchange of identical monomers. The symmetric and antisymmetric vibrations of the dimer play roles that are precisely analogous to the totally symmetric and Jahn-Teller active asymmetric vibrations of pseudo-Jahn–Teller systems (73–75). In the symmetric delocalized vibration, each corresponding stretch or bend has precisely the same amplitude and phase on both monomers, so both monomer energies go up and down together. This has no effect on energy transfer. In the antisymmetric delocalized vibration, each corresponding stretch or bend has precisely the same amplitude but opposite phase, so that one monomer's energy goes up while the other monomer's energy is going down. This causes decoherence and drives energy transfer by tuning the energy gap between excitons. Asymmetric means neither symmetric nor antisymmetric; for example, the  $b_{1g}$  or  $b_{2g}$  vibrations in the  $D_{4h}$  point group (which are symmetric under some point group rotations and antisymmetric under others) or the e vibrations in the  $C_{3v}$ point group (which are degenerate) are asymmetric (78). If the homodimer is nondegenerate, symmetry and antisymmetry generalize to correlated and anticorrelated vibrations that are inphase and out-of-phase, but may have unequal amplitudes (and are thus asymmetric).

# **Identifying Vibrational Symmetry with the Polarization Anisotropy**

Within the Franck–Condon principle (78), only totally symmetric vibrations are excited upon electronic excitation. The forbidden nontotally symmetric vibrations are usually weak in both the Raman effect and femtosecond vibrational wavepacket signals. However, only asymmetric vibrations can couple electronic states of different symmetries, and nonadiabatic coupling can excite large-amplitude antisymmetric vibrations in a dimer (79). In frequency domain Raman spectroscopy, the depolarization ratio can be used to determine vibrational symmetry (79a). In the time domain, vibrational symmetry can be identified through the polarization dependence of vibrational quantum beats. Khalil et al. (80) obtained depolarization ratios from off-resonant ground electronic state quantum beat amplitudes in liquid CCl<sub>4</sub>. Farrow et al. used the quantum beat polarization anisotropy (81) to identify symmetric and asymmetric vibrations on different electronic states at different stages of their electronic relaxation (82) through a Jahn–Teller conical intersection. In the large fourfold symmetric silicon naphthalocyanine molecule (SiNc) studied by Farrow et al., molecular rotation is slow, and electronic dynamics at the conical intersection drives the initial decay of the polarization anisotropy. In the aftermath of this nonadiabatic electronic process, vibrations persisted on the electronic ground state for picoseconds.

Vibrations can appear in the anisotropy if they modulate which polarization is absorbed—for example, increasing probe absorption polarized parallel to the pump while decreasing probe absorption polarized perpendicular to the pump and vice versa. In SiNc, three Jahn–Teller active asymmetric vibrations caused strong anisotropic quantum beats in precisely this manner. If a vibration modulates the parallel and perpendicular signals as

$$S(T) = \sum_{i} A_i f_i(T) + \sum_{\nu} A_{\nu} \cos(\omega_{\nu} T - \phi_{\nu}) f_{\nu}(T),$$
(new#6)

where the f(T) are monotonically decaying functions with  $f(0) \equiv 1$ , then the vibrational quantum beat anisotropy is defined by

$$r_{v} = \frac{A_{v\parallel} - A_{v\perp} \cos(\phi_{v\parallel} - \phi_{v\perp})}{A_{v\parallel} + 2A_{v\perp} \cos(\phi_{v\parallel} - \phi_{v\perp})}.$$
 (new#7)

A quantum beat's anisotropy depends on its two polarization-dependent amplitudes  $(A_{\nu\parallel},A_{\nu\perp})$  and phases  $(\phi_{\nu\parallel},\phi_{\nu\perp})$ . After the electronic coherence has decayed, two totally symmetric vibrations have  $r_{\nu}=1/10$  within error  $[A_{\nu\parallel}\approx (4/3)A_{\nu\perp}]$  with  $\phi_{\nu\parallel}\approx \phi_{\nu\perp}]$ , while the three anisotropic vibrations have  $r_{\nu}=\infty$  within error  $[A_{\nu\parallel}\approx 2A_{\nu\perp}]$  with  $\phi_{\nu\parallel}-\phi_{\nu\perp}\approx\pi$ , which causes a vanishing denominator]. The maximum amplitude of these vibrational quantum beats in the anisotropy is about 0.007 (81), well over an order of magnitude smaller than the excitonic anisotropy quantum beats reported by Savikhin et al. (61). The vibrational anisotropies match group theoretical predictions, based on the two-photon tensor, for vibrations on the ground electronic state.

# Polarization Insights into Coupled Vibrations and Electronic Dynamics

Are there vibrations on the excited electronic state? On the doubly degenerate excited electronic state, the Jahn–Teller effect nonadiabatically couples asymmetric vibrations and electronic excitations to form mixed vibrational-electronic or vibronic states. Totally symmetric vibrations are not coupled by the Jahn–Teller effect and can still be called vibrations. On the excited electronic state, vibronic and vibrational quantum beats have polarization anisotropies that are sensitive to electronic relaxation.

The strongest totally symmetric mode coherently vibrates on the ground and excited electronic states for picoseconds (81), but it has a time-dependent vibrational anisotropy consistent with excited-state electronic equilibration on a 200-fs timescale (81, 82). The picosecond survival of totally symmetric vibrations in the face of a 200-fs electronic equilibration can be understood because both excited-state adiabatic potential energy surfaces are exactly the same for totally symmetric coordinates; totally symmetric vibrations just lower their vibrational anisotropy as they equilibrate between excited electronic states. This measure of electronic equilibration has intriguing differences from that provided by the electronic polarization anisotropy (see 82, table 6).

In contrast, the predicted asymmetric quantum beat anisotropies would conflict with experiment if vibronic coherence survived much longer than indicated by the electronic and totally symmetric vibrational anisotropies; similarly, the asymmetric quantum beat phases would conflict with experiment if excited-state vibrational coherence survived (82). Importantly, the

asymmetric vibrations on the ground electronic state characterized the Jahn–Teller stabilization energies for the excited-state conical intersection, which accurately predicted the coherent electronic anisotropy over the first 100 fs (during which it decayed by 2/3) without any adjustable parameters (81). Just as symmetric vibrations on the ground electronic state can characterize the initial vibrational motion on a single excited electronic state (16), asymmetric vibrational quantum beats on the ground electronic state can characterize the initial electronic dynamics in Jahn–Teller coupled excited electronic states.

For SiNc, the asymmetric vibrational quantum beat amplitudes give Jahn-Teller stabilization energies on the order of a meV, which drive anisotropy decay on a 100 fs timescale. The corresponding Jahn-Teller distortions are much smaller than the range of vibrational zero point motion. The electronic dynamics at the Jahn-Teller conical intersection are remarkably fast for such a small driving energy.

Modeling the 2DFT spectra of SiNc showed that nonadiabatic Jahn–Teller dynamics destroys electronic coherence between the ground and excited states more slowly than it destroys the electronic alignment (83). In the Jahn–Teller model, coherent electronic interference could still occur after nonadiabatic electronic realignment of the emission dipole. As a result, the decoherence between the ground and excited electronic states (as measured by the antidiagonal cross-width in the 2DFT spectra) was dominated by low-frequency totally symmetric vibrational and solvent motion. This nonexponential decoherence was characterized with a Brownian oscillator model. The Brownian oscillator model is based on harmonic vibrations subject to damping and random forces that are linked by the fluctuation-dissipation theorem (15)(18, 70). The non-exponential damped parts of the response function indicate a 1/e decoherence time of ~180 fs, though it is probable that some of the damped response in the model represents low-frequency underdamped modes.

Similar pump–probe results were obtained in a free-base naphthalocyanine with  $D_{2h}$  symmetry (84). This molecule has a pseudo-Jahn–Teller effect (72, 85, 86) in which the x- and y-polarized electronic states are slightly split, but quasi-resonantly coupled by an asymmetric vibration. In this case, the v = 0 vibrational level of the lowest electronic state is isolated and does not completely equilibrate within 200 fs, but higher vibronic levels do. On the excited state, the vibrational motion has larger amplitude than the adiabatic potential surfaces would suggest and the direction of vibrational motion changes with the laser polarization in the molecular frame

(87). The pseudo-Jahn–Teller Hamiltonian can be transformed by an electronic basis set rotation so that it becomes the Hamiltonian for a degenerate homodimer (73, 74, 86). This transformation suggests similar mechanisms for decoherence in dimers.

# **QUANTUM BEATS IN ENERGY TRANSFER**

In 2007, Engel et al. (88) reported that 2DFT spectra of the photosynthetic FMO antenna protein exhibited quantum beats with an unexpectedly large amplitude (about 10% of the maximum 2D amplitude) and a lifetime exceeding 600 fs at 80 K. Since the Franck–Condon displacements of the bacteriochlorophyll *a* pigments in FMO are small (an order of magnitude less than the range of zero-point motion) (89, 90), it was argued that the protein must somehow be preserving electronic coherence between excitonic states beyond both the typical electronic decoherence timescale and the FMO energy transfer timescale. It was suggested that long-lived electronic coherence was functionally important for the high quantum efficiency of photosynthetic light harvesting (88). Many experiments were devised and carried out to test these hypotheses. Experiments on one-pigment proteins indicated that the coherence spans more than one pigment (91). Others indicated that Franck–Condon active vibrations of isolated bacteriochlorophyll *a* are too weak to explain the quantum beats (92). By late 2012, nine proposed 2DFT signatures of photosynthetic energy transfer had been reported in various antenna proteins (49, 93–96). The experiments had also spawned theoretical efforts to explain the underlying energy transfer (36, 97, 98).

## **Vibrational-Excitonic Resonance**

In a key paper, Womick & Moran (99) showed that resonance between a vibration and the electronic energy gap between two excitons increased the energy transfer rate in one phycocyanin by an order of magnitude compared to a phycocyanin without vibrational-excitonic resonance. The standard one-particle vibronic exciton model (100, 101) they used explicitly assumes that energy transfer from donor to acceptor excites a localized vibration on the excited electronic state of the acceptor. Their calculations used modified Redfield theory (101a) to treat relaxation, which requires weak system-bath couplings. Womick and Moran found that inclusion of the resonant vibration in the electronic system was critical; such inclusion implicitly assumes the vibrational-excitonic resonance interaction is stronger than the remaining system-bath

couplings. **Figure 3** shows that vibronic state to vibronic state energy transfer rate constants and excitonic delocalization sharply increase for vibrational-excitonic resonance.

## The Thick Plottens

At around this time, the experiments became even more puzzling. Improved 2DFT experiments showed that the oscillations lasted for picoseconds (95) and reported a  $\pi/2$  phase relationship between oscillations of the diagonal peaks and oscillations of the cross-peaks (95). This phase relationship could not be explained by electronic coherence, but it was suggested that it might be explained by a quantum transport process (102) in which energy flows between pigments and the environment (95). However, in the calculated 2D spectra for quantum transport (102), cross-peaks oscillated in phase with diagonal peaks. With the coherence lifetime in the usual realm for coherent vibrations, Christensson et al. (103) proposed that vibronic coherence might explain the long-lived quantum beats. These are modifications of the original electronic coherence hypothesis. Butkus et al. (104) showed that the  $\pi$  phase shift between opposite cross-peaks reported in Reference 94 was not a consequence of electronic coherence and could not be reproduced by electronic coherence models. At this point, no single hypothesis could explain all nine reported 2D signatures of photosynthetic energy transfer, and some reported signatures were unexplained.

# A Fully Alternative Hypothesis

In 2013, Tiwari et al. (105) proposed that vibrational-excitonic resonance on the excited state of photosynthetic antennas could amplify femtosecond Raman excitation of vibrations on the electronic ground state. This is what happens in the Jahn–Teller and pseudo-Jahn–Teller molecules, where asymmetric vibrational quantum beats bear a resemblance to electronic quantum beats, but live for picoseconds on the ground electronic state. It is the fully alternative hypothesis to that proposed in 2007 and explains beats with amplitude too large for Franck–Condon vibrations but lasting too long for electronic coherence by invoking nonadiabatic amplification of vibrations rather than preservation of electronic coherence.

This hypothesis was backed by nonadiabatic calculations of 2DFT spectra that used a dimer model with parameters based on the low-temperature absorption and emission spectra of the FMO protein and the Raman spectrum of its isolated pigment, bacteriochlorophyll *a*. These independently established a vibrational-excitonic resonance in FMO similar to that in

allophycocyanin. Tiwari et al. also included both donor and acceptor vibrations. This allows energy transfer in which the vibration is left behind on the ground electronic state of the donor (41, 105, 106). The relationship to the pseudo-Jahn–Teller Hamiltonian reveals that the key vibrations are delocalized over both pigments in the dimer: Correlated vibrations are analogous to totally symmetric vibrations and decoupled from the nonadiabatic dynamics; anticorrelated vibrations are analogous to asymmetric vibrations and coupled into the nonadiabatic dynamics. Correlated vibrations can survive energy transfer (106a) but derive their amplitude only from adiabatic potential energy surface displacement in accord with the Franck-Condon principle.

Figure 4 shows how localized coordinates are related to delocalized coordinates (41).

## **Anticorrelated Vibrations in Energy Transfer**

In a localized electronic and vibrational basis, the Hamiltonian for a nondegenerate homodimer with one vibration on each pigment can be written as

$$\hat{H} = \sum_{A,B} \frac{1}{2} \omega (\hat{q}_X^2 + \hat{p}_X^2) \hat{I} + \begin{bmatrix} (E^A - \omega d^A \hat{q}_A) & J \\ J & (E^B - \omega d^B \hat{q}_B) \end{bmatrix}.$$
 (6)new#8

Here,  $\omega$  is the common vibrational frequency for the two identical pigments;  $\hat{q}_A$  and  $\hat{q}_B$  ( $\hat{p}_A$  and  $\hat{p}_B$ ) are the vibrational coordinates (momenta) in the two pigments; and the pigments have localized electronic excitation energies  $E^A$  and  $E^B$ , localized displacements  $d^A$  and  $d^B$ , and a Coulombic coupling J. For large distances between pigments, the Coulombic coupling can be calculated from Förster's transition-dipole approximation. The difference  $\Delta = (E^B - E^A)$  between localized electronic excitation energies is caused by the protein, as is any difference between localized displacements. The energy gap between excitons is  $\Delta_{EX} = [\Delta^2 + 4J^2]^{1/2}$  ( $\Delta_{EX}$  should be used as the splitting  $\Delta$  in Eq. 1-5.) Transforming to the delocalized vibrational coordinates shown in Figure 4, this becomes

$$\hat{H} = \left(\sum_{+,-} \frac{1}{2} \omega(\hat{q}_{X}^{2} + \hat{p}_{X}^{2}) - \omega d_{+} \hat{q}_{+} - \omega(d_{-}^{AB}/2) \hat{q}_{-}\right) \hat{I} + \begin{bmatrix} (E^{A} + \omega(d_{-}^{A-B}/2) \hat{q}_{-}) & J \\ J & (E^{B} - \omega(d_{-}^{A-B}/2) \hat{q}_{-}) \end{bmatrix}.$$
 (7)new#9

Only the anticorrelated vibration  $q_{-}$  is involved in energy transfer; the correlated vibrational

coordinate  $q_+$  factors out. Conversely, the vibrational displacements for the anticorrelated coordinates are reduced by excitonic delocalization (and partially transformed into off-diagonal couplings), while the correlated vibrations are unaffected by excitonic delocalization (41, 106). Thus, correlated and anticorrelated coordinates provide a different perspective (41, 106) on the standard measures of excitonic delocalization (107, 108). Vibrational delocalization is driven by the energy transfer coupling.

The above discussion concentrates on intramolecular vibrations. The harmonic oscillator displacement is related to the Marcus reorganization energy  $\lambda = (1/2)\omega d^2$  and the Huang–Rhys factor  $S = d^2/2$ . Both can be summed to assess the total impact of all displaced vibrations. In the high-temperature limit, the total reorganization energy is half the Stokes shift between absorption and emission maxima. The total Huang–Rhys factor gives the vibrational overlap between zero-point states as  $\langle v^A = 0 | v^B = 0 \rangle = \exp(-S/2)$ . For bacteriochlorophyll a, intramolecular vibrations have a greater reorganization energy than the solvent, but the two have similar total Huang–Rhys factors ( $S \approx 0.3$ ) (109). Comparing S and  $\lambda$ , low-frequency modes of the solvent or protein environment have more impact on decoherence than they have on energetic stabilization. This is mitigated by the requirement that low frequency/long wavelength modes must impact pigments differently to have any effect on energy transfer (110).

Figure 5 shows the potentials and the real-valued nonadiabatic eigenstates of the dimer Hamiltonian as a function of the anticorrelated coordinate. The Hamiltonian parameters are  $\Delta=150~{\rm cm}^{-1},\ J=66~{\rm cm}^{-1},\ \omega=200~{\rm cm}^{-1},\ {\rm and}\ d^A=d^B\approx0.22$ . These give adiabatic electronic states separated by ~200 cm<sup>-1</sup> at  $q_-=0$ , so that the excitonic energy gap is resonant with the 200-cm<sup>-1</sup> vibrational frequency. The displacements upon electronic excitation are obtained from the Raman spectrum and are smaller than the classical turning points for zero-point vibration (  $q=\pm1$ ), so that the donor potential curve is nested inside the acceptor potential curve, forming a nested funnel. In order to show both the electronic and vibrational character of the nonadiabatic eigenfunctions  $\langle q_-|\psi_m\rangle=a_m(q_-)|A\rangle+b_m(q_-)|B\rangle$ , Figure 5 plots the overall vibrational amplitude

$$\Phi_m(q_-) = \sqrt{|a_m(q_-)|^2 + |b_m(q_-)|^2}$$

and uses color to show both the electronic character and sign of the eigenfunction at each coordinate

$$\Theta_m(q_-) \equiv \operatorname{atan2}[b_m(q_-), a_m(q_-)],$$

where atan2 is the extended arctangent function with a  $2\pi$  range from two arguments. Together, the vibrational amplitude and electronic angle show the complete nonadiabatic eigenfunction (87). This is a form of exact factorization (111–114), in which the vibrational amplitude acquires a nodeless character for strong nonadiabatic mixing. The resonant pairs of nonadiabatic eigenstates in Figure 5 have very similar nodeless vibrational amplitudes and strong variation in electronic character as a function of the anticorrelated coordinate.

The coordinate-dependent electronic character in **Figure 5** indicates a complete breakdown of Förster's adiabatic framework for energy transfer (105). In Förster's strong-coupling adiabatic limit, vibrational motion to coordinates with different electronic character is required for energy transfer (23), whereas in Förster's weak coupling nonadiabatic limit, vibrational motion to coordinates with a localized nonadiabatic coupling is required for energy transfer (23); in contrast, **Figure 5** shows that, with a vibrational-excitonic resonance, energy transfer can take place at all vibrational coordinates. There is no need for energetically costly vibrational motion with amplitude much larger than the zero point range of motion.

# Nonadiabatic Raman Enhancements in 2D Fourier Transform Spectra

This extensive mixing causes a nonadiabatic enhancement of the femtosecond Raman processes that excite coherent vibrations on the ground electronic state. **Figure 6** shows four wave-mixing energy ladder diagrams (115) that take into account the nonadiabatic coupling in **Figure 5** using the same color coding. The basis states for **Figure 6** have anticorrelated vibrations on localized electronic states. The diagrams are arranged to correspond to the four peaks in the 2D spectrum in **Figure 2**. In these diagrams, the length of the arrows indicates the transition frequency and the color of the arrows indicates the transition dipole direction for pigments A and B. The cross-peak labeled CP12 has a fully electronically allowed path in which all of the transition dipoles have strong  $\Delta v = 0$  Franck–Condon overlaps. In this pathway, the first field transfers some wavefunction amplitude to the excited electronic state using a  $v_- = 0$  to  $v_- = 0$  transition on the donor; nonadiabatic mixing with  $v_- = 1$  of the electronically excited acceptor allows the second

field to use a  $v_- = 1$  to  $v_- = 1$  transition to transfer some wavefunction amplitude to  $v_- = 1$  on the ground electronic state of the dimer (in which neither pigment is excited). The third pulse parallels the action of the first, and the radiated signal parallels the action of the second. During each of the three time intervals between molecule—field interactions, the molecular frequency can be read off as the signed difference between the energies at the heads of the last solid and dashed arrows. For these diagrams, the first (excitation) and second (relaxation) frequencies are both negative, while the third (detection) frequency is positive. Each diagram for Raman excitation of an anticorrelated vibration has the same excitation/detection frequencies and sequence of transition dipole directions as the corresponding diagram for electronic coherence on the excited state. This similarity shows how quantum beats from nonadiabatically excited anticorrelated vibrations could easily have been mistaken for quantum beats from electronic coherence.

Figure 6 also shows that the diagrams for Raman modulations of the other 2D peaks predict weaker beats because they contain  $\Delta v_{\perp} \neq 0$  transitions. It is well known that arguments based on a representative diagram can be misleading because diagrams often fully or partly cancel each other in the sum (18). However, calculated 2DFT spectra show that the predicted modulations are qualitatively correct. While the nonadiabatic Raman enhancement of anticorrelated vibrations resembles electronic coherence for the cross-peak in which the excitation frequency is greater than the detection frequency, the Raman enhancement is weaker for the other 2D peaks. In contrast to the electronic coherence hypothesis, Figure 6 predicts weak vibrational quantum beats on the diagonal peaks in the rephasing 2D spectrum. It also predicts that the anti-Stokes cross-peak (detection frequency magnitude greater than excitation frequency magnitude) is even weaker, while both cross-peaks should have the same strength for electronic coherence. These predictions for nonadiabatic Raman enhancement were in accord with unexplained aspects of prior experimental reports (94, 95). Investigation showed that all nine reported 2D signatures of photosynthetic energy transfer were predicted by nonadiabatic Raman enhancement of anticorrelated vibrations (105). Electronic coherence only accounts for five of them.

FMO subunits hold 7 bacteriochlorophyll *a* pigments in close proximity. Low-temperature absorption/circular dichroism and Raman/fluorescence line narrowing spectra also provide evidence for vibrational-excitonic resonances with a 165-cm<sup>-1</sup> gap (106). This establishes vibrational-excitonic resonance for both frequencies at which  $\sim \pi/2$  phase shifts for quantum beats on the diagonal peaks were reported by Engel and coworkers. This raises the question of

whether such resonances are common. For FMO, five distinct quantum beat frequencies had been reported on seven cross-peaks or shoulders in the 2DFT spectra. Within error, these matched the five observed Raman/Franck–Condon active vibrations of bacteriochlorophyll a in the same frequency range (105).

# No Evidence for Long-Lived Electronic Coherence

With this scenario, Tiwari et al. (105) calculated that in FMO, at the cryogenic temperature of 80K used for many experiments, 2DFT signatures of electronic coherence between excitons would inhomogeneously dephase on approximately the 160-fs timescale measured by Savikhin et al. (61), suggested that signatures of vibronic coherence might persist somewhat longer, and explained that anticorrelated vibrations on the ground electronic state could persist for picoseconds. With vibrational-excitonic resonance, the electronic, vibronic, and ground-state vibrational quantum beats all occur at approximately the same frequency. Crucially, the calculations by Tiwari et al. left no experimental evidence for long-lived electronic coherence in photosynthetic proteins. However, the inhomogeneous dephasing of 2DFT excitonic coherence signatures does not imply decay of the underlying excitonic coherence (in fact, there was no decay of the underlying electronic coherence in the model used by Tiwari et al.). Even without including this excitonic decoherence [which must be slower than the excitonic dephasing characterized by Savikhin et al. (61)] this calculation of the nonadiabatic Raman enhancement should be reasonably accurate because the time window for Raman excitation is limited by the ~100 fs timescale for optical decoherence between the ground and excited electronic states. Tiwari et al. included this optical decoherence phenomenologically by using a Brownian oscillator for correlated vibrational and environmental motions. However, the speed and efficiency of energy transfer between pigments depends on the interplay between the longer quantum population transfer time (~600 fs from the resonant splitting in Figure 5) and the timescales for vibrational relaxation (35), loss of vibrational anti-correlation (105), and single protein vibronic decoherence (41),.

## **Vibrational Aftermath**

The nonadiabatic calculation of anticorrelated beats on the electronic ground state in 2DFT spectra was soon confirmed by Plenio et al. (116). In 2014, Miller (117) and coworkers reported experiments in which they isolated vibronic coherence in the excited-state absorption region of

the 2DFT spectra for a degenerate bis-cyanine homodimer. This was the first report that isolated 2DFT signatures of excited-state coherence (118), and the reported vibronic dephasing lifetime was short (~80 fs at room temperature). This model system differs from the photosynthetic proteins because the vibrational displacements are larger in cyanines than in chlorophylls, so faster decoherence could be expected. A theoretical study by Mukamel and coworkers found reasonable agreement with the electronic dephasing time, calculated that picosecond-lived vibrations might be found in cyanine dimers, and suggested a similar picture for photosynthetic complexes (119).

Fleming and coworkers examined the effect of damped excitonic energy gap fluctuations on nonadiabatic enhancement of energy transfer and vibrations in the 2D spectra of a model dimer(120). Fluctuations were incorporated through bilinear coupling to a continuous harmonic bath (120a) that was chosen to rapidly damp excitonic coherence. [These bath parameters generate a larger Stokes' shift than is observed for stable FMO proteins (120b), thus speeding up decoherence.] Vibrational beats were resonantly enhanced in the calculated 2D spectra at 77K. However, these bath parameters did not yield a vibrational-excitonic resonance enhancement of the energy transfer (energy transfer is slower than Raman vibrational excitation and thus more susceptible to damped fluctuations), and both enhancements were suppressed by larger fluctuations at physiological temperatures. Fleming and co-workers concluded that the picosecond oscillations in the 2D spectra are vibrational, but that enhancement of vibrational beats in 2D spectra need not indicate vibrational enhancement of energy transfer (120). Lee and Troisi used a surrogate Hamiltonian with a discrete set of bath modes to include fluctuations of the energy transfer coupling (120c). With parameters chosen to model the phycocyanins studied by Womick and Moran (99), Lee and Troisi reported partial suppression of vibronic enhancement in the efficiency of energy transfer between pigments. At present, the interactions driving vibronic decoherence and relaxation still need to be carefully characterized in order to assess whether specific vibrational-excitonic resonances play a significant role in energy transfer for any given system,.

For the photosystem II (PS II) reaction center of higher plants, which performs the primary charge separation in oxygenic photosynthesis (121), the Ogilvie (122) and van Grondelle (123) groups simultaneously reported systematic coincidences between vibrational frequencies and excitonic energy gaps in 2D oscillation maps. For reasons that are not yet clear, the frequencies

reported by the two groups for PS II do not all agree. Although prior work indicated larger, nonspecific couplings in the primary charge transfer of bacterial photosynthesis (124), both groups discussed a 120-cm<sup>-1</sup> or 127-cm<sup>-1</sup> frequency as possibly vibronic and suggested vibrational-excitonic resonances might be important for charge transfer in PS II.

A report of long-lived (picosecond) coherence in two-color three-pulse echoes from oxidized bacterial reaction centers was interpreted in terms of vibrational-excitonic resonance amplifying femtosecond Raman excitation of ground-state vibrations (125). This assignment was based on the 100-fs lifetime for the excited state of the oxidized special pair. However, the 2DFT spectra for this system show beats of equal amplitude on both cross-peaks (126). This implicates generation via the excited electronic state, not the Raman mechanism discussed above for FMO. Paleček et al. (126) proposed that energy transfer from the accessory bacteriochlorophyll donor to the oxidized special pair acceptor leaves the ground state of the donor coherently vibrating (as for a vibrational-excitonic resonance), and have named this process ETICS, (energy transfer—induced coherence shift). It is not clear whether there is vibrational resonance with the donor—acceptor electronic energy gap in this system or how general ETICS is.

# **2D OSCILLATION MAPS**

The true 3D Fourier transform electronic spectra measured by Turner et al. (127) could be manipulated to view slices showing 2D electronic spectra as a function of Raman frequency. Later, Davis et al. (128) used phase retrieval to obtain a series of 2D spectra for positive relaxation times and Fourier transformed the series with respect to *T*. This produced a similar set of 2D oscillation maps showing the amplitude and phase of relaxation time oscillations across the 2D spectrum. The set has three frequency dimensions (two electronic and one Raman) and can be manipulated via projections and slices (3, 13, 129) like a 3DFT spectrum (130). The Raman dimension can show frequencies for vibrational coherences on either the ground or excited electronic states, for excitonic coherences between excitons with the same number of excitations, or vibronic coherences between vibrations on different excitons. A variety of 2D oscillation maps are possible depending on the type of 2D spectrum [absorptive/refractive (96), rephasing (95, 130, 131), or nonrephasing (130, 131)] and on whether the real (95) or complex (96, 131) 2D data set is transformed. Mančal et al. (132) developed theory for oscillations from excitonic and weak Franck–Condon active vibrations in 2D spectra. Butkus et al. (104) Fourier

transformed the real part of separate rephasing and nonrephasing 2D spectra to develop 2D oscillation map signatures for excitonic, vibronic, and vibrational coherences. As suggested by some of the frequencies involved in Figure 6, some 2D oscillations can require that the excitation pulse spectra have amplitude outside the frequency range of the 2D spectra used for the map; this can generate insidious filtering effects on 2D oscillation maps (132a). 2D oscillation maps have been used to study aggregates (133) and photosynthetic systems (122, 123, 126, 134–136).

In rephasing 2D oscillation maps, electronic, vibronic, and vibrational coherences are expected to have different signatures when the frequencies are separated (104, 137). Electronic quantum beats are expected to have equal amplitudes, the same phase, and opposite frequencies on opposite sides of the diagonal. In the low-temperature limit, vibrational quantum beats on the ground electronic state occur only on the Stokes side of the diagonal, while vibrational quantum beats on the excited electronic state occur on both sides of the diagonal, like electronic coherence. As a result, vibrational quantum beats have asymmetric 2D oscillation maps. Vibronic quantum beats with a mixed character can occur at a frequency equal to the difference between the vibrational frequency and the excitonic energy gap frequency. **Figure 7** illustrates these features of 2D oscillation maps for a molecular nanoring (133).

Duan et al. (138) reported 2D oscillation maps for FMO at an ambient temperature of 296 K that show a number of frequencies above  $\sim 600 \text{ cm}^{-1}$ , but no lower frequencies. They assign the observed frequencies to weak bacteriochlorophyll a molecular vibrations. Their reported 2DFT spectrum at T=0 has a very similar cross-width to that of SiNc (83) at room temperature, which is reasonable given the structural and electronic similarities between SiNc and bacteriochlorophyll a pigments.

Recently, Zigmantas and coworkers ( $\underline{135}$ ) obtained rephasing 2D oscillation maps for FMO at 77 K using the all-parallel and double-crossed polarization sequences. Oscillations at ~170 cm<sup>-1</sup> and ~210 cm<sup>-1</sup>, which coincide with both vibrations and excitonic energy gaps, are prominent. For both polarization sequences, quantum beats that decay with an ~100-fs time constant appear with similarly large amplitudes on both sides of the diagonal. These were assigned to electronic coherence. The all-parallel maps are dominated by fairly sharp 2D peaks with negative frequencies ( $-170 \text{ cm}^{-1}$  and  $-210 \text{ cm}^{-1}$ ) on the Stokes side of the diagonal. These quantum beats persist for about 2 ps. Their assignment to vibrations on the ground electronic state is supported by the square pattern of peaks predicted in Reference  $\underline{104}$ . In contrast, the

double-crossed maps have quantum beats that persist for ~600 fs and an asymmetry that favors the Stokes side of the diagonal, with a slightly weaker peak on the anti-Stokes side. These were assigned to vibronic coherence on the excited state, but the calculated 2D maps do not yet reproduce their amplitude on the anti-Stokes side of the diagonal [the calculations included only one explicitly coupled vibration per pigment and used the single-particle approximation of the vibronic-exciton model (100, 101), which has systematic errors that grow with vibrational quantum number (106)]. A second puzzle (contrasting with the ambient temperature results of Reference 138) is that predicted high-frequency vibrational modes (included in the calculations as Brownian oscillators) are absent in the experiment. Further investigation of the beats assigned to vibronic coherence may shed additional light on the timescale and energetic amplitude for environmental fluctuations that determine how important nonadiabatic couplings and vibrational-excitonic resonances are for the energy transfer process in FMO. Overall, this study appears to provide a startling confirmation of the scenario outlined by Tiwari et al. in reference 105.

*Note added in proof:* A recent paper describes use of mutagenesis to alter the excitonic structure of FMO. (143) Two pump-probe quantum beat frequencies (160 and 195 cm<sup>-1</sup>) with picosecond dephasing times were reported for all-parallel polarization. The authors concluded that both arose from vibrations on the ground electronic state.

## **CONCLUSION**

There has been substantial progress in understanding the 2DFT spectra of nonadiabatically coupled states in molecules, dimers, and photosynthetic complexes. The maximal nonadiabatic Raman enhancement of vibrational amplitudes on the ground electronic state requires only that vibronic coherence between resonant vibrational-excitonic states survive longer than optical coherence between the ground and excited electronic states. This criterion is readily met, and the resulting resonantly amplified vibrational coherences have provided vital evidence for a widespread photosynthetic coupling. Subsequent studies on several systems (including some of the same systems in which long-lived electronic coherence was initially reported) have concluded that the longest lived oscillations in the 2D spectra arise from vibrational coherence (119)(120)(125)(126)(133)(138), though it is not yet proven that all of these reported vibrations are delocalized or amplified by resonant couplings. Polarization studies and comparisons to the

isolated pigments should be useful for quantifying vibrational delocalization and amplification of anticorrelated vibrations. The question of whether vibronic coherence survives long enough for optimal nonadiabatic energy transfer through vibrational-excitonic resonances is not yet settled, and will depend on the various vibrational and correlation relaxation mechanisms that localize energy transfer on the acceptor. Investigations that focus on the shorter-lived excited-state coherences will be vital in refining hypotheses about efficient energy transfer in natural and artificial systems. Work so far points to a new nonadiabatic energy transfer regime that lies outside the adiabatic framework for energy transfer developed by Förster. With vibrational-electronic resonances, large-amplitude motions are not required for fast nonadiabatic electronic transitions. Similar nonadiabatic regimes are likely to be relevant for many charge transfer and internal conversion processes.

## DISCLOSURE STATEMENT

The author is not aware of any affiliations, memberships, funding, or financial holdings that might be perceived as affecting the objectivity of this review.

## **ACKNOWLEDGMENTS**

Andy Moran, Vytautas Butkus, and Donatas Zigmantas generously provided figures for this review. I am grateful to the members of my research group, especially Wei Qian, Darcie Farrow, Eric Ryan Smith, Katherine Kitney-Hayes, William Peters, Vivek Tiwari, and Peter Foster, for their ongoing efforts to reveal how nonadiabatic dynamics work at low vibrational velocity. This material is based upon work supported by the National Science Foundation under grant CHE-1405050 and by the Air Force Office of Scientific Research under award FA9550-14-1-0258. Any opinions, findings, and conclusions or recommendations expressed in this material are those of the author and do not necessarily reflect the views of the National Science Foundation.

#### LITERATURE CITED

- 1. Hybl JD, Albrecht AW, Gallagher Faeder SM, Jonas DM. 1998. Two-dimensional electronic spectroscopy. *Chem. Phys. Lett.* 297:307–13
- 1a. Zhang WM, Chernyak V, Mukamel S. 1999. Multidimensional femtosecond correlation spectroscopies of electronic and vibrational excitons. *J. Chem. Phys.* 110:5011-28
- 4. Gallagher Faeder SM, Jonas DM. 1999. Two-dimensional electronic correlation and relaxation spectra: theory and model calculations. *J. Phys. Chem. A* 103:10489–505
- 2. Hybl JD, Albrecht Ferro A, Jonas DM. 2001. Two-dimensional Fourier transform electronic spectroscopy. *J. Chem. Phys.* 115:6606–22
- 3. Jonas DM. 2003. Two-dimensional femtosecond spectroscopy. *Annu. Rev. Phys. Chem.* 54:425–63
- 5. Michl J. 1972. Photochemical reactions of large molecules. I. A simple physical model of photochemical reactivity. *Mol. Photochem.* 4:243–57
- 6. Zimmerman HE. 1972. MO following: the molecular orbital counterpart of electron pushing. *Acc. Chem. Res.* 5:393–401
- 7. Marcus RA. 1993. Electron transfer reactions in chemistry: theory and experiment (Nobel lecture). *Angew. Chem.* 32:1111–21
- 8. Zewail AH. 1988. Femtochemistry. Science 242:1645-53
- 9. Fragnito HL, Bigot J-Y, Becker PC, Shank CV. 1989. Evolution of the vibronic absorption spectrum in a molecule following impulsive excitation with a 6 fs optical pulse. *Chem. Phys. Lett.* 160:101–4
- 10. Nelson KA, Williams L. 1987. Femtosecond time-resolved observation of coherent molecular vibrational motion. *Phys. Rev. Lett.* 58:745
- 11. Rosker MJ, Wise FW, Tang CL. 1986. Femtosecond relaxation dynamics of large molecules. *Phys. Rev. Lett.* 57:321–24
- 12. Hybl JD, Christophe Y, Jonas DM. 2001. Peak shapes in femtosecond 2D correlation spectroscopy. *Chem. Phys.* 266:295–309
- 13. Ernst RR, Bodenhausen G, Wokaun A. 1987. *Principles of Nuclear Magnetic Resonance in One and Two Dimensions*. Oxford: Oxford Univ. Press
- 14. Bernstein RB, Zewail AH. 1989. Femtosecond real-time probing of reactions. III. Inversion to the potential from femtosecond transition state spectroscopy experiments. *J. Chem. Phys.*

- 90:829-42
- 15. Mukamel S. 1990. Femtosecond optical spectroscopy: a direct look at elementary chemical events. *Annu. Rev. Phys. Chem.* 41:647–81
- 16. Pollard WT, Mathies RA. 1992. Analysis of femtosecond dynamic absorption spectra of nonstationary states. *Annu. Rev. Phys. Chem.* 43:497–523
- 17. Jonas DM, Bradforth SE, Passino SA, Fleming GR. 1995. Femtosecond wavepacket spectroscopy: influence of temperature, wavelength, and pulse duration. *J. Phys. Chem.* 99:2594–608
- 18. Mukamel S. 1995. *Principles of Nonlinear Optical Spectroscopy*. New York: Oxford Univ. Press
- 19. Hybl JD, Gallagher Faeder SM, Albrecht AW, Tolbert CA, Green DC, Jonas DM. 2000. Time and frequency resolved femtosecond solvent dynamics. *J. Lumin.* 87–89:126–29
- 20. Hybl JD, Yu A, Farrow D, Jonas DM. 2002. Polar solvation dynamics in the femtosecond evolution of two dimensional spectra. *J. Phys. Chem. A* 106:7651–54
- 21. Mukamel S, Abramavicius D. 2004. Many-body approaches for simulating coherent nonlinear spectroscopies of electronic and vibrational excitons. *Chem. Rev.* 104:2073–98
- 22. Fuller FD, Ogilvie JP. 2015. Experimental implementations of two-dimensional Fourier transform electronic spectroscopy. *Annu. Rev. Phys. Chem.* 66:667–90
- 23. Förster T. 1965. Delocalized excitation and excitation transfer. In *Modern Quantum Chemistry*, ed. O Sinanoğlu III, pp. 93–137. New York: Academic
- 23a. Scholes GD. 2003. Long-Range Resonance Energy Transfer in Molecular Systems. *Annu. Rev. Phys. Chem.* 54:57-87
- 24. Lu HP, Xun L, Xie XS. 1998. Single-molecule enzymatic dynamics. Science 282:1877–82
- 25. Moerner WE, Fromm DP. 2003. Methods of single-molecule fluorescence spectroscopy and microscopy. *Rev. Sci. Instrum.* 74:3597–619
- 26. Moerner WE. 2015. Single-molecule spectroscopy, imaging, and photocontrol: foundations for super-resolution microscopy (Nobel lecture). *Angew. Chem. Int. Edit.* 54:8067–93
- 27. Landau LD, Lifschitz EM. 1977. Quantum Mechanics. New York: Pergamon
- 28. Cohen-Tannoudji C, Diu B, Laloë F. 1977. Quantum Mechanics. Paris: Wiley-Interscience
- 29. Zurek WH. 1982. Environment-induced superselection rules. *Phys. Rev. D* 26:1862–80
- 30. Caldeira AO, Leggett AJ. 1985. Influence of damping on quantum interference: an exactly

- soluble model. Phys. Rev. A 31:1059-66
- 31. Stern A, Aharonov Y, Imry Y. 1990. Phase uncertainty and loss of interference: a general picture. *Phys. Rev. A* 41:3436–48
- 32. Prezhdo OV, Rossky PJ. 1998. Relationship between quantum decoherence times and solvation dynamics in condensed phase chemical systems. *Phys. Rev. Lett.* 81:5294–97
- 33. Cohen-Tannoudji C, Diu B, Lalöe F. 1977. *Quantum Mechanics*. Paris: Wiley-Interscience. See pp. 1284–321 and pp. 339–42
- 34. Reimers JR, McKemmish LK, McKenzie RH, Hush NS. 2015. Nonadiabatic effects in thermochemistry, spectroscopy and kinetics: the general importance of all three Born–Oppenheimer breakdown corrections. *Phys. Chem. Chem. Phys.* 17:24641–65
- 35. Davydov AS, Serikov AA. 1972. Energy transfer between impurity molecules of a crystal in the presence of relaxation. *Phys. Stat. Sol. B* 51:57–68
- 36. Jang S, Cheng YC, Reichman DR, Eaves JD. 2008. Theory of coherent resonance energy transfer. *J. Chem. Phys.* 129:101104
- 37. Killoran N, Huelga SF, Plenio MB. 2015. Enhancing light-harvesting power with coherent vibrational interactions: a quantum heat engine picture. *J. Chem. Phys.* 143:155102
- 38. Prezhdo OV, Rossky PJ. 1997. Evaluation of quantum transition rates from quantum-classical molecular dynamics simulations. *J. Chem. Phys.* 107:5863–78
- 39. Hwang H, Rossky PJ. 2004. Electronic decoherence induced by intramolecular vibrational motions in a betaine dye molecule. *J. Phys. Chem. B* 108:6723–32
- 40. Becker PC, Fragnito HL, Bigot JY, Brito Cruz CH, Fork RL, Shank CV. 1989. Femtosecond photon echoes from molecules in solution. *Phys. Rev. Lett.* 63:505–7
- 41. Tiwari V, Peters WK, Jonas DM. 2017. Electronic energy transfer through non-adiabatic vibrational-electronic resonance. I. Theory for a dimer. *J. Chem. Phys.* 147:154308
- 42. Butcher PN, Cotter D. 1991. *The Elements of Nonlinear Optics*. New York: Cambridge Univ. Press
- 43. Zilian A, Wright JC. 1996. Polarization effects in four-wave mixing of isotropic samples. *Mol. Phys.* 87:1261–71
- 44. Fleming GR. 1986. *Chemical Applications of Ultrafast Spectroscopy*. New York: Oxford Univ. Press
- 45. Zare RN. 1988. Angular Momentum: Understanding Spatial Aspects in Physics and

- Chemistry. New York: Wiley-Interscience
- 46. Fourkas JT, Trebino R, Fayer MD. 1992. The grating decomposition method: a new approach for understanding polarization-selective transient grating experiments. I. Theory. *J. Chem. Phys.* 97:69–77
- 47. Williams S, Rahn LA, Zare RN. 1996. Effects of different population, orientation, and alignment relaxation rates in resonant four-wave mixing. *J. Chem. Phys.* 104:3947–55
- 48. Hochstrasser RM. 2001. Two-dimensional IR-spectroscopy: polarization anisotropy effects. *Chem. Phys.* 266:273–84
- 49. Schlau-Cohen GS, Ishizaki A, Calhoun TR, Ginsberg NS, Ballottari M, et al. 2012. Elucidation of the timescales and origins of quantum electronic coherence in LHCII. *Nat. Chem.* 4:389–95
- 50. Qian W, Jonas DM. 2003. Role of cyclic sets of transition dipoles in the pump–probe polarization anisotropy: application to square symmetric molecules and chromophore pairs. *J. Chem. Phys.* 119:1611–22
- 51. Monson PR, McClain WM. 1970. Polarization dependence of the two-photon absorption of tumbling molecules with application to liquid 1-chloronaphthalene and benzene. *J. Chem. Phys.* 53:29–37
- 52. McClain WM. 1971. Excited state symmetry assignment through polarized two-photon absorption studies of fluids. *J. Chem. Phys.* 55:2789–96
- 53. Corney A, Series GW. 1964. Theory of resonance fluorescence excited by modulated or pulsed light. *Proc. Phys. Soc.* 83:207–12
- 54. Dodd JN, Kaul RD, Warrington JM. 1964. The modulation of resonance fluorescence excited by pulsed light. *Proc. Phys. Soc.* 84:176–78
- 55. Aleksandrov EB, Kozlov VP. 1964. The theory of luminescence modulation, due the interference of coherent excited non-degenerate states. *Opt. Spektrosk.* 16:533–35
- 56. Aleksandrov EB. 1964. Luminescence beats induced by pulse excitation of coherent states. *Opt. Spektrosk.* 17:957–60
- 57. Letokhov VS, Chebotayev VP. 1977. *Nonlinear Laser Spectroscopy*. New York: Springer-Verlag
- 58. Demtröder W. 1982. Laser Spectroscopy. New York: Springer-Verlag
- 59. Shen YR. 1984. The Principles of Nonlinear Optics. New York: Wiley-Interscience

- 60. Walmsley IA, Mitsunaga M, Tang CL. 1988. Theory of quantum beats in optical transmission correlation and pump-probe experiments for general Raman configuration. *Phys. Rev. A* 38:4681–89
- 61. Savikhin S, Buck DR, Struve WS. 1997. Oscillating anisotropies in a bacteriochlorophyll protein: evidence for quantum beating between exciton levels. *Chem. Phys.* 223:303–12
- 63. Wynne K, Hochstrasser RM. 1993. Coherence effects in the anisotropy of optical experiments. *Chem. Phys.* 171:179–88. Erratum. 1993. *Chem. Phys.* 173:539
- 65. Sung J, Silbey RJ. 2001. Four wave mixing spectroscopy for a multilevel system. *J. Chem. Phys.* 115:9266–87. Erratum. 2005. *J. Chem. Phys.* 122:169901
- 66. Smith ER, Farrow DA, Jonas DM. 2005. Response functions for dimers and square symmetric molecules in four-wave-mixing experiments with polarized light. *J. Chem. Phys.* 123:044102. Publisher's Note. 2005. *J. Chem. Phys.* 123:179902. Erratum. 2008. *J. Chem. Phys.* 128:109902
- 69. Gu Y, Widom A, Champion PM. 1994. Spectral line shapes of damped quantum oscillators: applications to biomolecules. *J. Chem. Phys.* 100:2547–60
- 70. Tanimura Y, Mukamel S. 1993. Real-time path integral approach to quantum coherence and dephasing in nonadiabatic transitions and nonlinear optical response. *Phys. Rev. E* 47:118–36
- 71. Jahn HA, Teller E. 1937. Stability of polyatomic molecules in degenerate electronic states. I. orbital degeneracy. *Proc. R. Soc. Lond. A* 161:220–35
- 72. Öpik U, Pryce MHL. 1957. Studies of the Jahn–Teller effect I. A survey of the static problem. *Proc. R. Soc. Lond. A* 238:425–47
- 73. Witkowski A, Moffitt W. 1960. electronic spectra of dimers: derivation of the fundamental vibronic equation. *J. Chem. Phys.* 33:872–75
- 74. Fulton RL, Gouterman M. 1961. Vibronic coupling. I. Mathematical treatment for 2 electronic states. *J. Chem. Phys.* 35:1059–71
- 75. Fulton RL, Gouterman M. 1964. Vibronic coupling. II. Spectra of dimers. *J. Chem. Phys.* 41:2280–86
- 76. Robinson GW, Frosch RP. 1963. Electronic excitation transfer and relaxation. *J. Chem. Phys.* 38:1187–203
- 77. Birks JB. 1970. Photophysics of Aromatic Molecules. New York: Wiley-Interscience
- 78. Herzberg GH. 1991. Electronic Spectra of Polyatomic Molecules. Malabar, FL: Krieger

- 79. Friesner R, Silbey R. 1981. Exciton-phonon coupling in a dimer: an analytical approximation for eigenvalues and eigenvectors. *J. Chem. Phys.* 74:1166–74
- 79a. Herzberg GH. 1991. *Infrared and Raman Spectra of Polyatomic Molecules*. Malabar, FL: Krieger
- 80. Khalil M, Golonzka O, Demirdöven N, Fecko CJ, Tokmakoff A. 2000. Polarization-selective femtosecond Raman spectroscopy of isotropic and anisotropic vibrational dynamics in liquids. *Chem. Phys. Lett.* 321:231–37
- 81. Farrow DA, Qian W, Smith ER, Ferro AA, Jonas DM. 2008. Polarized pump–probe measurements of electronic motion via a conical intersection. *J. Chem. Phys.* 128:144510
- 82. Farrow DA, Smith ER, Qian W, Jonas DM. 2008. The polarization anisotropy of vibrational quantum beats in resonant pump-probe experiments: diagrammatic calculations for square symmetric molecules. *J. Chem. Phys.* 129:174509
- 83. Kitney-Hayes KA, Albrecht-Ferro AW, Tiwari V, Jonas DM. 2014. Two-dimensional Fourier transform electronic spectroscopy at a conical intersection. *J. Chem. Phys.* 140:124312
- 84. Peters WK, Smith ER, Jonas DM. 2011. Femtosecond pump-probe polarization spectroscopy of vibronic dynamics at conical intersections and funnels. In *Conical Intersections Theory: Computation and Experiment*, ed. W Domcke, DR Yarkony, H Köppel, pp. 715–45. Singapore: World Sci.
- 85. Bersuker IB. 2006. The Jahn-Teller Effect. Cambridge, UK: Cambridge Univ. Press
- 86. Englman R. 1972. *The Jahn–Teller Effect in Molecules and Crystals*. London: Wiley-Interscience
- 87. Peters WK, Tiwari V, Jonas DM. 2017. Nodeless vibrational amplitudes and quantum nonadiabatic dynamics in the nested funnel for a pseudo Jahn–Teller molecule or homodimer. *J. Chem. Phys.* 147:194306
- 88. Engel GS, Calhoun TR, Read EL, Ahn T-K, Mančal T, et al. 2007. Evidence for wavelike energy transfer through quantum coherence in photosynthetic systems. *Nature* 446:782–86
- 89. Diers JR, Bocian DF. 1995. Q<sub>y</sub>-excitation resonance Raman spectra of bacteriochlorophyll observed under fluorescence-free conditions. Implications for cofactor structure in photosynthetic proteins. *J. Am. Chem. Soc.* 117:6629–30
- 90. Rätsep M, Freiberg A. 2007. Electron-phonon and vibronic couplings in the FMO

- bacteriochlorophyll *a* antenna complex studied by difference fluorescence line narrowing. *J. Lumin.* 127:251–59
- 91. Wong CY, Alvey RM, Turner DB, Wilk KE, Bryant DA, et al. 2012. Electronic coherence lineshapes reveal hidden excitonic correlations in photosynthetic light harvesting. *Nat. Chem.* 4:396–404
- 92. Fransted KA, Caram JR, Hayes D, Engel GS. 2012. Two-dimensional electronic spectroscopy of bacteriochlorophyll *a* in solution: elucidating the coherence dynamics of the Fenna–Matthews–Olson complex using its chromophore as a control. *J. Chem. Phys.* 137:125101
- 93. Calhoun TR, Ginsberg NS, Schlau-Cohen GS, Cheng YC, Ballottari M, et al. 2009. Quantum coherence enabled determination of the energy landscape in light-harvesting complex II. *J. Phys. Chem. B* 113:16291–95
- 94. Collini E, Wong CY, Wilk KE, Curmi PMG, Brumer P, Scholes GD. 2010. Coherently wired light-harvesting in photosynthetic marine algae at ambient temperature. *Nature* 463:644–47
- 95. Panitchayangkoon G, Voronine DV, Abramavicius D, Caram JR, Lewis NHC, et al. 2011. Direct evidence of quantum transport in photosynthetic light-harvesting complexes. *PNAS* 108:20908–12
- 96. Turner DB, Dinshaw R, Lee K-K, Belsley MS, Wilk KE, et al. 2012. Quantitative investigations of quantum coherence for a light-harvesting protein at conditions simulating photosynthesis. *Phys. Chem. Chem. Phys.* 14:4857–74
- 97. Chin AW, Datta A, Caruso F, Huelga SF, Plenio MB. 2008. Noise-assisted energy transfer in quantum networks and light harvesting complexes. *New J. Phys.* 12:065002
- 98. Hoyer SH, Sarovar M, Whaley KB. 2010. Limits of quantum speedup in photosynthetic light harvesting. *New J. Phys.* 12:065401
- 99. Womick JM, Moran AM. 2011. Vibronic enhancement of exciton sizes and energy transport in photosynthetic complexes. *J. Phys. Chem. B* 115:1347–56
- 100. Philpott MR. 1967. Vibronic coupling in the exciton states of the rigid-lattice model of molecular crystals. *J. Chem. Phys.* 47:4437–45
- 101. Roden J, Eisfeld A, Briggs JS. 2008. The J- and H-bands of dye aggregate spectra: analysis of the coherent exciton scattering (CES) approximation. *Chem. Phys.* 352:258–66
- 101a. Yang M, Fleming GR. 2002. Influence of phonons on exciton transfer dynamics:

- comparison of Redfield, Förster, and modified Redfield equations. Chem. Phys. 282:163-80
- 102. Abramavicius D, Mukamel S. 2010. Quantum oscillatory exciton migration in photosynthetic reaction centers. *J. Chem. Phys.* 133:064510
- 103. Christensson N, Kauffmann HF, Pullerits T, Mančal T. 2012. Origin of long lived coherences in light-harvesting complexes. *J. Phys. Chem. B* 116:7449–54
- 104. Butkus V, Zigmantas D, Valkunas L, Abramavicius D. 2012. Vibrational versus electronic coherences in 2D spectrum of molecular systems. *Chem. Phys. Lett.* 545:40–43
- 105. Tiwari V, Peters WK, Jonas DM. 2013. Electronic resonance with anticorrelated pigment vibrations drives photosynthetic energy transfer outside the adiabatic framework. *PNAS* 110:1203–8
- 106. Tiwari V, Jonas DM. 2018. Electronic energy transfer through non-adiabatic vibrational-electronic resonance. II. 1D spectra for a dimer. *J. Chem. Phys.* 148: 084308. Publisher's Note, *J. Chem. Phys.* 148:119901
- 106a. Cina JA, Fleming GR. 2004. Vibrational coherence transfer and trapping as sources for long-lived quantum beats in polarized emission from energy transfer complexes. *J. Phys. Chem. A* 108:11196-208
- 107. Spano FC. 2009. The spectral signatures of Frenkel polarons in H- and J-aggregates. *Acc. Chem. Res.* 43:429–39
- 108. Spano FC, Yamagata H. 2011. Vibronic coupling in J-aggregates and beyond: a direct means of determining the exciton coherence length from the photoluminescence spectrum. *J. Phys. Chem. B* 115:5133–43
- 109. Rätsep M, Cai Z-L, Reimers JR, Freiberg A. 2011. Demonstration and interpretation of significant asymmetry in the low-resolution and high-resolution Q<sub>y</sub> fluorescence and absorption spectra of bacteriochlorophyll *a. J. Chem. Phys.* 134:024506
- 110. Soules TF, Duke CB. 1971. Resonant energy transfer between localized electronic states in a crystal. *Phys. Rev. B* 3:262–74
- 111. Hunter G. 1975. Conditional probability amplitudes in wave mechanics. *Int. J. Quantum Chem.* 9:237–42
- 112. Czub J, Wolniewicz L. 1978. On the non-adiabatic potentials in diatomic molecules. *Mol. Phys.* 36:1301–8
- 113. Cederbaum LS. 2013. The exact molecular wavefunction as a product of an electronic and a

- nuclear wavefunction. J. Chem. Phys. 138:224110
- 114. Gidopoulos NI, Gross EKU. 2014. Electronic non-adiabatic states: towards a density functional theory beyond the Born–Oppenheimer approximation. *Phil. Trans. R. Soc. A* 372:20130059
- 115. Lee D, Albrecht AC. 1993. On global energy conservation in nonlinear light–matter interaction: the nonlinear spectroscopies, active and passive. *Adv. Chem. Phys.* 83:43–87
- 116. Plenio MB, Almeida J, Huelga SF. 2013. Origin of long-lived oscillations in 2D-spectra of a quantum vibronic model: electronic versus vibrational coherence. *J. Chem. Phys.* 139:235102
- 117. Halpin A, Johnson PJM, Tempelaar R, Murphy RS, Knoester J, et al. 2014. Two-dimensional spectroscopy of a molecular dimer unveils the effects of vibronic coupling on exciton coherences. *Nat. Chem.* 6:196–201
- 118. Tiwari V, Peters WK, Jonas DM. 2014. Vibronic coherence unveiled. Nat. Chem. 6:173–75
- 119. Duan HG, Nalbach P, Prokhorenko VI, Mukamel S, Thorwart M. 2015. On the origin of oscillations in two-dimensional spectra of excitonically-coupled molecular systems. *New J. Phys.* 17:072002
- 120. Fujihashi Y, Fleming GR, Ishizaki A. 2015. Impact of environmentally induced fluctuations on quantum mechanically mixed electronic and vibrational pigment states in photosynthetic energy transfer and 2D electronic spectra. *J. Chem. Phys.* 142:212403
- 120a. Tanaka M, Tanimura Y. 2009. Quantum Dissipative Dynamics of Electron Transfer Reaction System: Nonperturbative Hierarchy Equations Approach. J. Phys. Soc. Jpn. 78:073802
- 120b. Kell A, Acharya K, Blankenship RE, Jankowiak R. 2014. On destabilization of the Fenna–Matthews–Olson complex of *Chlorobaculum tepidum*. *Photosynth. Res.* 120:323-9
- 120c. Lee MH, Troisi A. 2017. Vibronic enhancement of excitation energy transport: Interplay between local and non-local exciton-phonon interactions. *J. Chem. Phys.* 146:075101
- 121. Blankenship RE. 2002. *Molecular Mechanisms of Photosynthesis*. Oxford, UK: Blackwell Sci.
- 122. Fuller FD, Pan J, Gelzinis A, Butkus V, Senlik SS, et al. 2014. Vibronic coherence in oxygenic photosynthesis. *Nat. Chem.* 6:706–11
- 123. Romero E, Augulis R, Novoderezhkin VI, Ferretti M, Thieme J, et al. 2014. Quantum coherence in photosynthesis for efficient solar-energy conversion. *Nat. Phys.* 10:677–83

- 124. Lathrop EJP, Friesner RA. 1994. Simulation of optical spectra from the reaction center of *Rb. sphaeroides*. Effects of an internal charge-separated state of the special pair. *J. Phys. Chem.* 98:3056–66
- 125. Ryu IS, Dong H, Fleming GR. 2014. Role of electronic-vibrational mixing in enhancing vibrational coherences in the ground electronic states of photosynthetic bacterial reaction center. *J. Phys. Chem. B* 118:1381–88
- 126. Paleček D, Edlund P, Westenhoff S, Zigmantas D. 2017. Quantum coherence as a witness of vibronically hot energy transfer in bacterial reaction center. *Sci. Adv.* 3:1603141
- 127. Turner DB, Stone KW, Gundogdu K, Nelson KA. 2009. Three-dimensional electronic spectroscopy of excitons in GaAs quantum wells. *J. Chem. Phys.* 131:144510
- 128. Davis JA, Hall CR, Dao LV, Nugent KA, Quiney HM, et al. 2011. Three-dimensional electronic spectroscopy of excitons in asymmetric double quantum wells. *J. Chem. Phys.* 135:044510
- 129. Bracewell RN. 2000. The Fourier Transform and its Applications. Boston: McGraw Hill
- 130. Li H, Bristow ADB, Siemens ME, Moody G, Cundiff ST. 2013. Unraveling quantum pathways using optical 3D Fourier-transform spectroscopy. *Nat. Commun.* 4:1390
- 131. Seibt J, Hansen T, Pullerits Tn. 2013. 3D spectroscopy of vibrational coherences in quantum dots: theory. *J. Phys. Chem. B* 117:11124–33
- 132. Mančal T, Christensson N, Lukeš V, Milota F, Bixner O, et al. 2012. System-dependent signatures of electronic and vibrational coherences in electronic two-dimensional spectra. *J. Phys. Chem. Lett.* 3:1497–502
- 132a. Camargo FVdeA, Grimmelsmann L, Anderson HL, Meech SR, Heisler IA. 2017.
  Resolving Vibrational from Electronic Coherences in Two-Dimensional Electronic
  Spectroscopy: The Role of the Laser Spectrum. *Phys. Rev. Lett.* 118:033001
- 133. Butkus V, Alster JA, Bašinskaitė E, Augulis R, Neuhaus P, et al. 2017. Discrimination of diverse coherences allows identification of electronic transitions of a molecular nanoring. *J. Phys. Chem. Lett.* 8:2344–49
- 134. Ferretti M, Novoderezhkin VI, Romero E, Augulis R, Pandit A, et al. 2014. The nature of coherences in the B820 bacteriochlorophyll dimer revealed by two-dimensional electronic spectroscopy. *Phys. Chem. Chem. Phys.* 16:9930–39
- 135. Thyrhaug E, Tempelaar R, Alcocer MA, Zídek K, Bína D, et al. 2017. Unravelling

- coherences in the FMO complex. arXiv:1709.00318v1 [physics.chem-ph] (submitted to Nat. Chem.)
- 136. Dostál J, Mančal T, Vácha F, Pšenčík J, Zigmantas DZ. 2014. Unraveling the nature of coherent beatings in chlorosomes. *J. Chem. Phys.* 140:115103
- 137. Butkus V, Valkunas L, Abramavicius D. 2014. Vibronic phenomena and exciton—vibrational interference in two-dimensional spectra of molecular aggregates. *J. Chem. Phys.* 140:034306
- 138. Duan H-G, Prokhorenko VI, Cogdell RJ, Ashraf K, Stevens AL, et al. 2017. Nature does not rely on long-lived electronic quantum coherence for photosynthetic energy transfer. *PNAS* 114:8493–98
- 139. Maiuri M, Ostroumov EE, Saer RG, Blankenship RE, Scholes GD 2018. Coherent wavepackets in the Fenna Matthews-Olson complex are robust to excitonic-structure perturbations caused by mutagenesis. *Nat. Chem.* 10:177-183

## SIDEBAR: DECOHERENCE

Decoherence refers to the decay in magnitude for an off-diagonal element of the reduced density matrix of the system (32). This reduced density matrix definition involves only one system, not an ensemble average. For a coupled system and bath, decoherence between two states of the system arises from the partial trace over bath degrees of freedom used to generate the reduced density matrix of the system alone,  $\hat{\rho}_S(t) = \text{Tr}_B[\hat{\rho}(t)]$ . Mathematically, decoherence arises from either bath-induced relative phase uncertainty for the system or system-induced changes in bath overlap (39, 40). (The uncertainty arises from phase variation with bath coordinates.) We define a positive real-valued decoherence function between states R and P of a system S as

$$D_{S}^{RP}(t) = \frac{\left|\left\langle R \middle| \hat{\rho}_{S}(t) \middle| P \right\rangle\right|}{\left\langle R \middle| \hat{\rho}_{S}(t) \middle| R \right\rangle^{1/2} \left\langle P \middle| \hat{\rho}_{S}(t) \middle| P \right\rangle^{1/2}}.$$

This definition has precedent in References 30, 31, though others omit the absolute value (38, 39). This decoherence function decays with the possibility of interference between reactants R and products P, independent of the extent of reaction. It can be used to prove that transferring degrees of freedom from the bath to the system slows decoherence between the more completely specified system states. As a corollary, if the electronic states and initial conditions are the same, vibronic decoherence is always slower than electronic decoherence (41).

## TERMS AND DEFINITIONS

**Adiabatic:** separable vibrational-electronic states in which the electronic wavefunction depends only on the vibrational coordinates

**Anisotropy:** for linearly polarized excitation, the ratio  $r(t) = [||(t) - \bot(t)|]/[||(t) + 2\bot(t)]$  calculated from the signals for parallel and perpendicular probing

**Asymmetric vibration**: asymmetric vibrational coordinates have an (antisymmetric) sign change under some point group rotation operations but are unchanged (symmetric) under others **Dephasing:** the decay of an oscillatory signal from an ensemble by both decoherence and the addition of signals with different frequencies

Exciton: an excited electronic state that is delocalized over more than one pigment

**Funnel:** a region of potential energy surfaces where nonadiabatic transitions between electronic states are faster than vibrational relaxation

Figure 1 Pulse sequence for two-dimensional Fourier transform (2DFT) spectroscopy. Three noncollinear pulses a, b, c generate a nonlinear polarization with wavevector  $\hat{\mathbf{k}}_p = \hat{\mathbf{k}}_c + \hat{\mathbf{k}}_b - \hat{\mathbf{k}}_a$ , which radiates the signal field. The pulse centers arrive at the sample at times  $t_a$ ,  $t_b$ , and  $t_c \equiv 0$ . The time interval  $\tau \equiv t_b - t_a$  between the first two pulses is positive for rephasing 2D spectra, negative for nonrephasing 2D spectra, and scanned over both positive and negative delays to obtain 2D correlation and relaxation spectra with real absorption peak shapes and imaginary refraction peak shapes. The relaxation time  $T \equiv \min(|t_a|,|t_b|)$  is held fixed during a 2D scan [T = 0 for a 2D correlation spectrum]. A 2DFT spectrum is obtained by Fourier transformation of each signal field with respect to the time t (conjugate to the detection frequency  $\omega_t$ ) and Fourier transformation of the array of signals with respect to  $\tau$  (conjugate to the excitation frequency  $\omega_\tau$ ).

Figure 2 Real part of the ground electronic state contribution to the rephasing two-dimensional (2D) electronic spectrum for a model dimer at a temperature of 80 K. The vertical axis is the excitation frequency  $-\omega_t$ , and the horizontal axis is the detection frequency  $\omega_t$ . The amplitude of the 2D spectrum for each frequency pair is indicated by color and via contours at the 0, 2, 4, 6, 8, 10–90% levels. Positive and negative contours are solid and dashed, respectively. The relaxation time is T = 0 fs. The 2D spectra are dominated by four resolved peaks, which oscillate in amplitude and shape with T. Diagonal peak maxima are marked with an o; cross-peak maxima are marked with an x. Figure adapted from Reference 105.

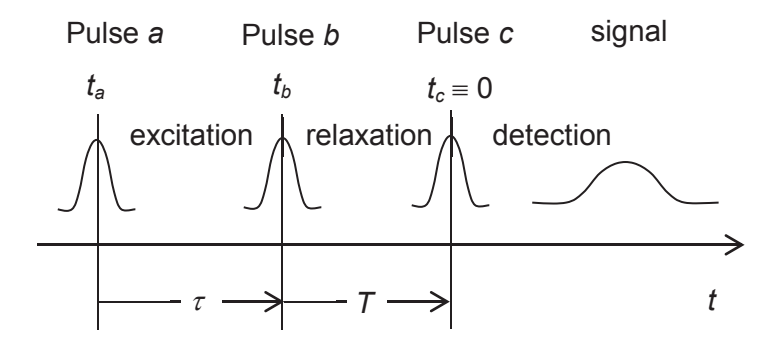
Figure 3 (a) Energy transfer rate constants from modified Redfield theory for allophycocyanin (APC) and C-phycocyanin (CPC) as a function of the dimer electronic energy gap. The state-to-state rate constants were computed using a one-particle vibronic exciton Hamiltonian. Subscripts 1–4 indicate delocalized vibrational-excitonic states derived from localized basis states with energies  $E_{\beta}$ ,  $E_{\beta} + \hbar \omega$ ,  $E_{\alpha}$ , and  $E_{\alpha} + \hbar \omega$ , respectively. On the rate constants, the rightmost subscript indicates the initial state and the leftmost subscript indicates the final state. (b) Participation ratios for vibrational-excitonic states (calculated from equation 16 of Reference 99) show excitonic delocalization for all states (1–4) through purely excitonic resonance at zero dimer electronic energy gap and delocalization for states 2 and 3 through their vibrational-excitonic resonance when the dimer electronic energy gap matches a vibrational quantum. Empirical site energy differences for APC and CPC, shown in purple, indicate a vibrational-excitonic resonance in APC. Figure adapted from Reference 99 with permission. Copyright 2011 American Chemical Society.

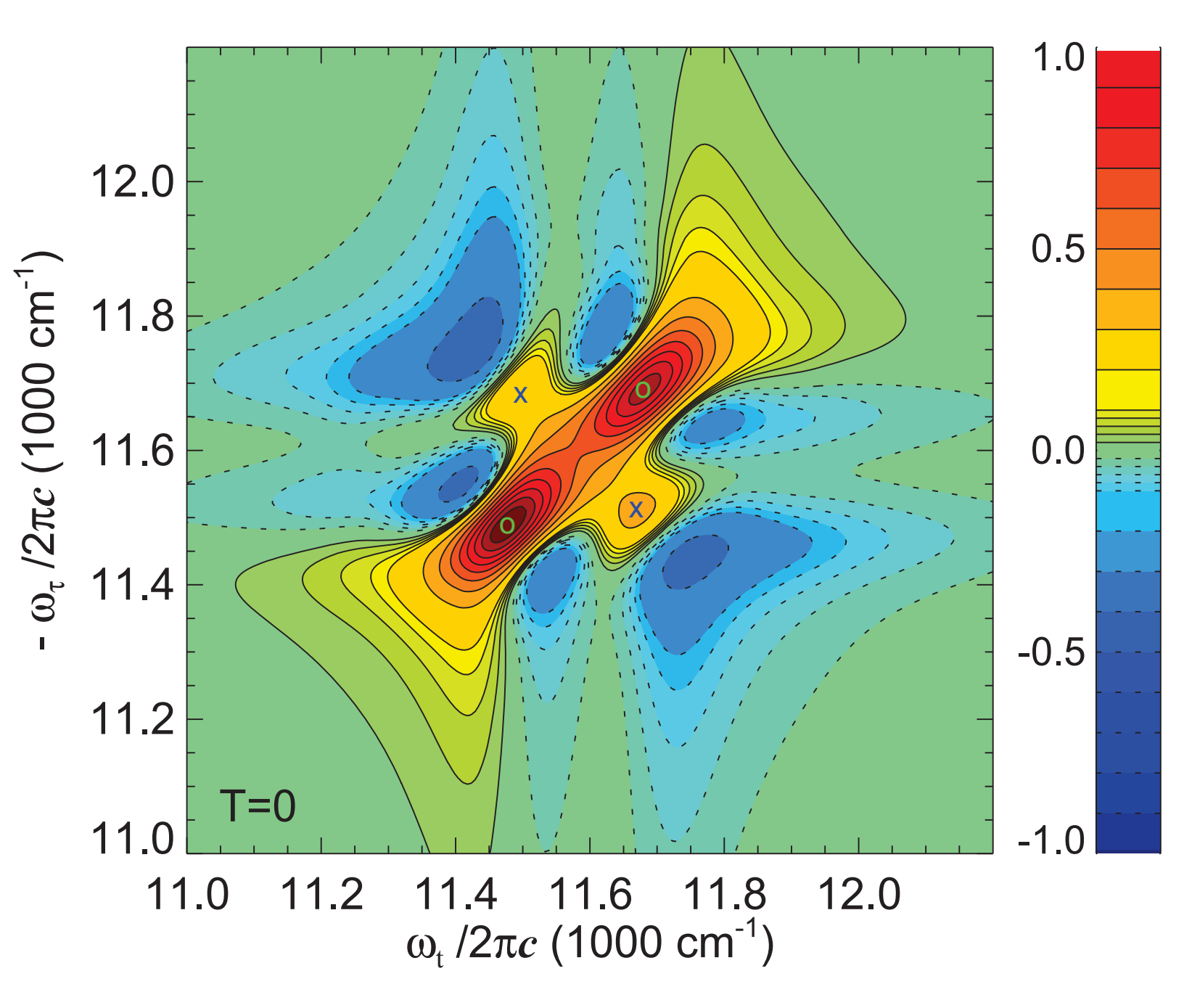
Figure 4 Geometrical relationships between vibrational coordinates localized on each pigment and the delocalized correlated and anticorrelated vibrational coordinates for unequal pigment displacements. Here,  $q_A$  and  $q_B$  mark the displacements of the localized vibrations on pigments A and B from the equilibrium geometry of the ground electronic state at (0,0). The equilibrium intramolecular vibrational coordinates of pigments A and B in their localized electronically excited states are  $(q_A, q_B) = (d^A, 0)$  and  $(0, d^B)$ , respectively. The doubly excited electronic state has equilibrium vibrational coordinate  $(d^A, d^B)$ . The anticorrelated coordinate  $q_-$  is defined by the gradient in the A-B electronic energy gap and parallel to the diagonal with length  $d_-^{A-B}$ . The correlated coordinate  $q_+$  is perpendicular to the anticorrelated coordinate; motion along  $q_+$  causes no change in the A-B electronic energy gap. In the  $(q_+, q_-)$  coordinate system, the doubly excited electronic state has equilibrium coordinate  $(2d_+, d_-^{AB})$ , and the excited states localized on A and B have equilibrium coordinates of  $[d_+, (d_-^{AB} + d_-^{A-B})/2]$  and  $[d_+, (d_-^{AB} - d_-^{A-B})/2]$ , respectively. With excitonic mixing angle  $\theta_d$ , this spacing shrinks from  $d_-^{A-B}$  to  $d_-^{A-B}$  cos $(2\theta_d)$ , moving the exciton minima symmetrically inward to the locations  $d^\alpha$  and  $d^\beta$  marked with crosses. Adapted from Reference 41 with permission from AIP Publishing.

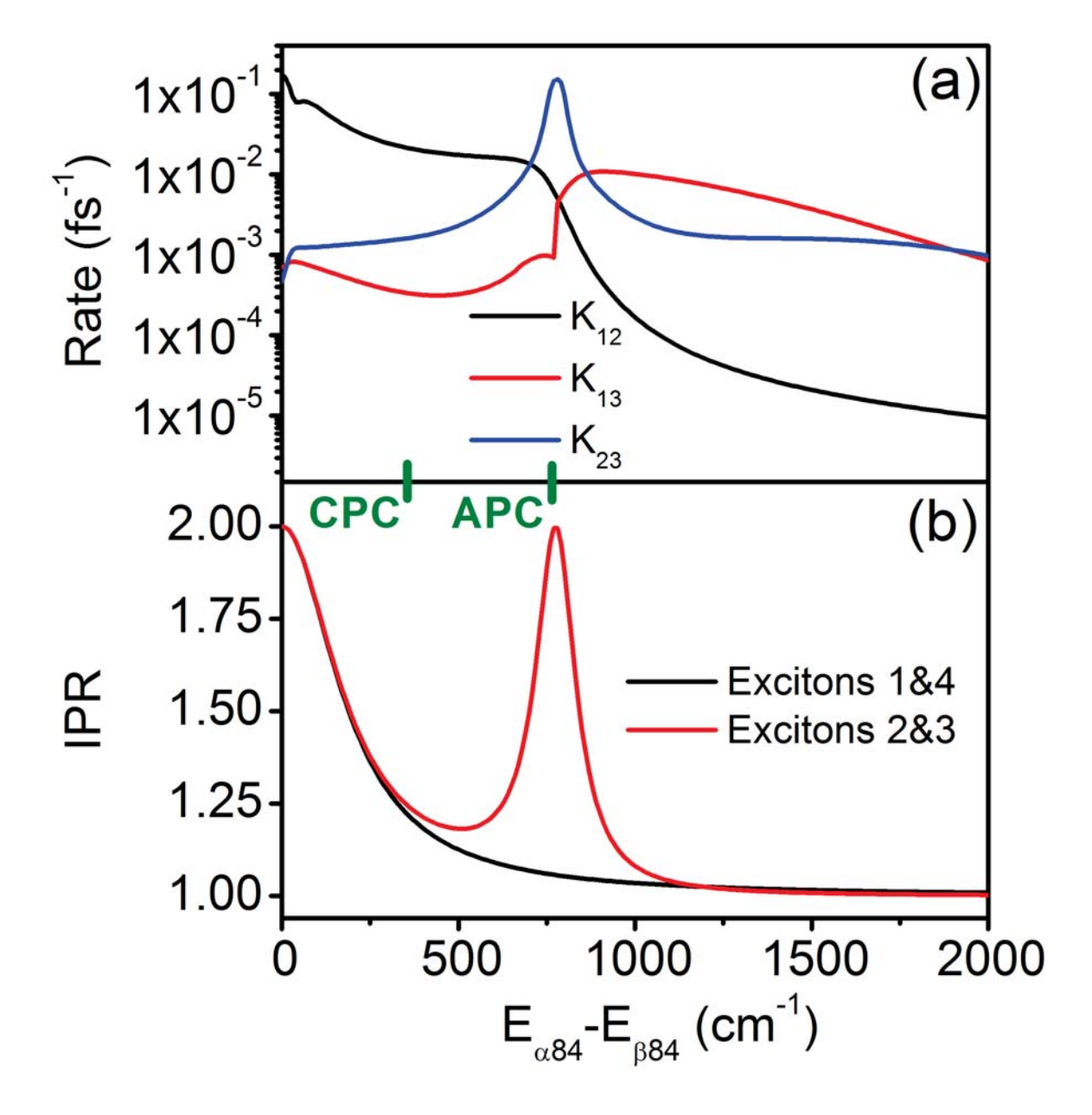
Figure 5 A vibrational-excitonic resonance for energy transfer. (a) The uncoupled donor and acceptor potential energy surfaces are shown as functions of the anticorrelated vibrational coordinate  $q_-$ , with the donor B in orange and the acceptor A in purple (see color wheel in panel d). Vibrational energy levels are marked by dotted lines, and corresponding eigenfunctions are shown. The donor and acceptor curves are split by an energy gap  $\Delta$ . (b) In the adiabatic approximation, the coupled donor (red) and acceptor (indigo) form partially delocalized exciton states with an avoided crossing between potential curves at upper left, a larger energy gap  $\Delta_{EX}$ , and resonant vibrational energy levels shown as coincident red and indigodotted lines. (c) The exact nonadiabatic states of the coupled system have nodeless vibrational amplitudes and strong variation in electronic character (as indicated by the color wheel in panel d) with coordinate. (d) Color wheel corresponding to panels a-c.

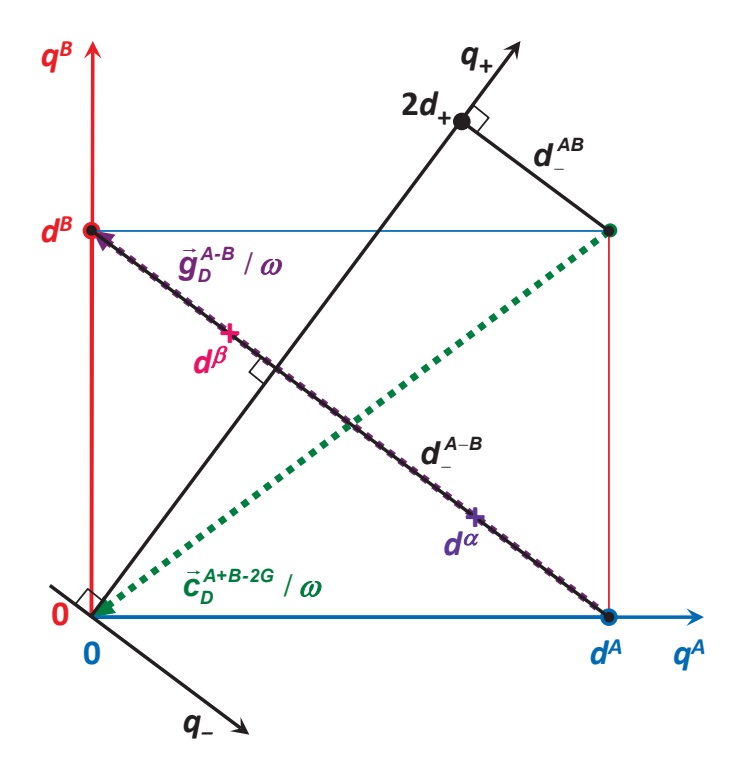
Figure 6 Wave-mixing pathways for the oscillatory ground state two-dimensional (2D) signal (D<sub>3</sub> in Reference 3) showing resonant enhancement by nonadiabatic coupling of vibrational and electronic levels. For each diagram, the vertical axis is energy and time runs from left to right (neither drawn to scale). The pathways are arranged to correspond with peaks in the rephasing 2D spectrum (Figure 2). Delocalized, anticorrelated vibrational levels on each electronic state are indicated by solid lines for  $v_{-}=0$ , dashed lines for  $v_{-}=1$ , and dotted lines for  $v_{-}=2$ ; their purple and orange colors indicate localized electronic basis states on pigments A and B, respectively. As in Figure 5, resonant pairs of levels couple to form the nonadiabatic states [the first pair is roughly  $(|A\rangle|v_-=1\rangle\pm|B\rangle|v_-=0\rangle)/2^{1/2}$ ]. The purple (or orange) vertical lines in the figure represent field–matter interactions utilizing the A (or B) electronic character of a mixed level, with no change in  $V_{-}$ , yielding a vibrational overlap integral approaching one. Thus, the cross-peak at upper left is fully electronically enhanced at every step, with all frequencies and transition dipole directions matching those for purely electronic coherence. Vertical lines in black represent weaker field–matter interactions; these have small vibrational overlap or lack vibrational-electronic resonance. As a result, oscillations of the other three peaks are not fully electronically enhanced. Figure adapted from Reference 105.

Figure 7 Coherences revealed by absolute value two-dimensional (2D) oscillation maps obtained from rephasing 2D Fourier transfer (FT) spectra from a nanoring of six covalently linked porphyrins. Dashed vertical and horizontal lines indicate transition frequencies for five of the six excitonic states. Calculations including only the second and third lowest excitons (top row) are compared to experiment (bottom row). The oscillation amplitude at each point of a map is indicated by the color bar. Each 2D oscillation map is independently normalized to its maximum amplitude. Contours show the rephasing 2DFT spectrum at waiting time T = 30 fs. In contrast to Figure 2, the excitation frequency axis is horizontal and the detection frequency axis is vertical. (a) Oscillation maps for the electronic coherence at  $\omega_2 = \pm 615 \text{ cm}^{-1}$ . To show the symmetry across the diagonal, the maps were obtained by Fourier transforming the real part of the rephasing 2DFT spectra with respect to the waiting time. (b) Vibrational coherences at  $\omega_2$  =  $-380 \text{ cm}^{-1}$  and  $\omega_2 = +380 \text{ cm}^{-1}$ . These maps were obtained by Fourier transforming the complex-valued rephasing 2DFT spectra in order to separate frequencies that are signed relative to the positive sign of  $\omega_3$  and negative sign of  $\omega_1$ . (c) Vibronic coherences at  $\omega_2 = -235$  cm<sup>-1</sup> and  $\omega_2 = +235 \text{ cm}^{-1}$ . In each panel, dashed lines parallel to the diagonal are separated by  $\omega_2$ . Figure adapted from Reference 133 with permission. Copyright 2017 American Chemical Society.









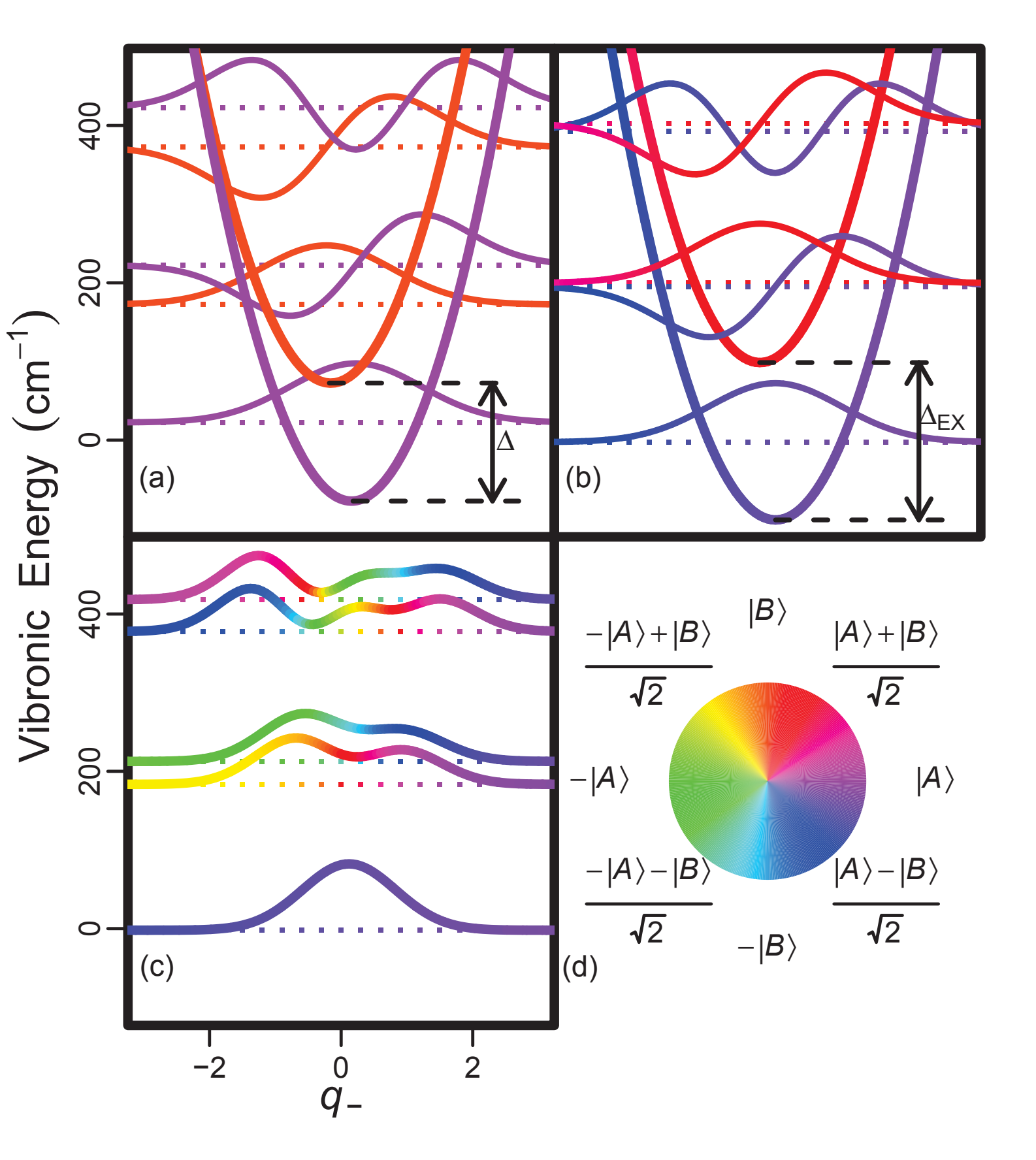


Figure 5

